High-Throughput Computational Screening of Two-Dimensional Semiconductors and Heterostructures for Photocatalytic Applications

V. Wang,[1, *] G. Tang,[2] R. T. Wang,[1] Y. C. Liu,[1] Y. Y. Liang,[3] Y. Kawazoe,[4, 5, 6] J. Nara,[7] and W. T. Geng[8, †]
[1]*Department of Applied Physics, Xi'an University of Technology, Xi'an 710054, China*
[2]*Advanced Research Institute of Multidisciplinary Science,*
Beijing Institute of Technology, Beijing 100081, China
[3]*Department of Physics, Shanghai Normal University, Shanghai 200234, China*
[4]*New Industry Creation Hatchery Center, Tohoku University, Sendai, Miyagi 980-8579, Japan*
[5]*Department of Physics and Nanotechnology, SRM Institute of*
Science and Technology, Kattankulathur,Tamil Nadu-603203, India
[6]*Department of Physics, Suranaree University of Technology, Nakhon, Ratchasima, Thailand*
[7]*National Institute for Materials Science, Tsukuba 305-0044, Japan*
[8]*School of Materials Science and Engineering, Hainan University, Haikou 570228, China*
(Dated: July 23, 2022)

By performing high-throughput first-principles calculations combined with a semiempirical van der Waals dispersion correction, we have screened 74 direct- and 184 indirect-gap two dimensional (2D) nonmagnetic semiconductors from near 1000 monolayers according to the criteria for energetic, thermodynamic, mechanical, dynamic and thermal stabilities, and conductivity type. We present the calculated lattice constants, simulated scanning tunnel microscopy, formation energy, Young's modulus, Poisson's ratio, shear modulus, anisotropic effective mass, band structure, band gap, ionization energy, and electron affinity for each candidate meeting our criteria. The resulting 2D semiconductor database (2DSdb) can be accessed via the website `https://materialsdb.cn/2dsdb/index.html` or invoking the VASPKIT program [Comput. Phys. Commun. 267, 108033 (2021)]. We also provide the calculated periodic table of band alignment type for van der Waals heterostructures when packing any two of the 200 screened semiconductor monolayers to form bilayers. Based on the rules of thumb for photocatalytic water splitting, we have further screened dozens of potential semiconductors and thousands of heterostructures from 2DSdb which are promising for photocatalytic water splitting. The 2DSdb provides an ideal platform for computational modeling and design of new 2D semiconductors and heterostructures in photocatalysis, nanoscale devices, and other applications.

I. INTRODUCTION

Since the successful isolation of graphene,[1,2] two dimensional (2D) materials have attracted tremendous attentions due to their novel electronic, optical, thermal, and mechanical properties for potential applications in a great variety of fields. Owing to the quantum confinement effect along the out-of plane direction, 2D materials often exhibit unique features, different from those of their bulk counterparts.[3–15] For examples, an unusual half-integer quantum Hall effect was observed in graphene.[7] The electronic properties of transition-metal dichalcogenides (TMDs) with MX_2 composition (where M = Mo or W and X = S, Se or Te) can be tuned from metallic to semiconducting by controlling layer-thickness.[6,8,15–18] The peculiar puckered honeycomb structure of few-layer black phosphorene (BP) leads to significant anisotropic electronic and optical properties on zigzag and armchair directions.[14,19,20] Remarkably, its band gap is also thickness-dependent, varying from 0.3 eV in the bulk limit to ∼2.2 eV in a monolayer with a direct band gap character. Other 2D materials, such as hexagonal boron nitride (*h*-BN),[21] silicene,[22–25] germanene,[26,27] stanene,[28] also exhibit many exotic characteristics that are absent in their bulk form.

A common feature of 2D materials is that they are formed by stacking layers with strong in-plane bonds and weak, van der Waals (vdW)-like interlayer attraction with typical binding energies of dozens of meV, allowing exfoliation into individual and atomically thin layers. This means that 2D materials usually possess in-plane stability in the absence of dangling bonds, in contrast to bulk films that are plagued by dangling bonds and surface state. Inspired by this feature, Inoshita *et al.* screened the potential 2D binary stoichiometric electrides from the layered crystal structures by performing first-principles calculations based on the density functional theory (DFT) within the generalized gradient approximation (GGA).[29] Later, Ahston and co-workers used a topology-scaling algorithm combining high-throughput calculations to uncover more than 800 monolayers based on the Materials Project crystal structure databases.[30,31] Considering the fact that the semi-local density functionals such as GGA functional significantly overestimates the lattice constants of crystals having vdW bonds. A rough thumb rule is that if the relative error in lattice constant *a* or *b* or *c* (experimental versus GGA-calculated) of one bulk phase is larger than 5%, it might have 2D structure. Choudhary *et al.* identified at least 1300 monolayers by comparing the experimental lattice constants with those predicted using the GGA functional.[32] Cheon *et al.* also identified thousand of 2D layered materials based on data mining algorithm.[33] Another important database for 2D materials was builded by Mounet *et al.*[34] They chose the binding energy obtained by DFT calculations with the vdW correction as the screening criterion ($\leq$ few tens of meV$\cdot$Å^{-1}) and identified more than 1800 structures. There are several 2D crystals databases publicly available at present, such as MC2D,[34] C2DB[35], 2DMatPedia[36] and JARVIS-DFT[32]. However, one of the major limitations of these databases is that they mainly focus on the stability analysis and provide only a small number of the fundamental physical properties such as lattice constants, formation energy, exfoliation energy, and band gap at the GGA level. Although the GGA functional can provide sufficiently accurate results on forces, structures, and band dispersions, it underestimates band gap of semiconductors, averagely by 50%.

In parallel with the efforts on synthesis of new 2D materials, another strategy has been gaining strength over the past few years. By stacking together different 2D materials on top of each other, various artificial heterostructures which is known as vdW heterostructures (vdWHs) can be formed.[37,38] Compared with the conventional bulk semiconductor-based heterostructures which require similar lattice structures of the components, vdWHs do not demand crystal lattice matching. One can build artificial vdWHs with desired functionalities by picking and stacking atomic layers of arbitrary compositions. The vdWHs not only preserve the excellent properties of the original single layers due to the weak vdW interaction, but also bear additional features. The invention of vdWHs has enriched greatly the variety of materials and also served as a powerful material platform for exploring new physics and developing exotic devices in nanoscale. There are numerous review articles highlight their potential applications in electronics,[39] photonics,[40] spintronics,[41] superconductivity,[42] energy storage,[43] catalysis,[44] etc. Despite their widespread applications, a systematic high-throughput investigation of a wide range of vdWHs is still incomplete, to the best of our knowledge.

In this work, combined the high-throughput first-principles calculations with a semiempirical van der Waals dispersion correction, we have chosen the energetic, thermodynamic, mechanical, dynamic, thermal stabilities and conductivity type as the criteria and screened around 260 2D semiconductors from near 1000 structures. We here present the lattice constants, formation energy, scanning tunnel microscopy (STM), Young's modulus, Poisson's ratio, phonon dispersions, band structure, effective masses of carriers, band gap, ionization energy and electron affinity for each candidate. In addition, the periodic table of heterostructure types including more than 20000 possible vdWHs is also presented. Since 2D semiconductors and vdWHs have demonstrated unprecedented performance and ability in the field of photocatalysis thanks to their large specific surface area, readily tunable electronic properties, sufficient adsorption and catalytic sites, high carrier mobility and short carrier migration distance compared to bulk photocatalysts,[45–47] the potential 2D semiconductors and vdWHs for photocatalytic water splitting have been further screened. The remainder of this paper is organized as follows. In Sec. II, methodology and computational details are described. The details of screening criteria are discussed in Sec. III. Sec. IV presents the calculations of structural, mechanical and electronic properties. Finally, a short summary is given in Sec. V.

II. METHODOLOGY

A. Density functional calculations

Our total energy calculations were performed using the Vienna Ab initio Simulation Package (VASP).[48,49] The electron-ion interaction was described using projector augmented wave (PAW) method[50,51] and the exchange and correlation (XC) were treated with GGA in the Perdew Burke Ernzerhof (PBE) form[52]. Part of electronic structure calculations were also performed using the standard screening parameter of Heyd-Scuseria-Ernzerhof (HSE06) hybrid functional,[53–58] upon the PBE-calculated equilibrium geometries. A cutoff energy of 400 eV was adopted for the plane wave basis set, which yields total energy convergence better than 1 meV/atom. In addition, the non-bonding vdW interaction is incorporated by employing a semi-empirical correction scheme of Grimme's DFT-D2 method in this study, which has been successful in describing the geometries of various layered materials.[59,60] In the slab model of 2D systems, periodic slabs were separated by a vacuum layer of 20 Å in z direction to avoid mirror interactions. The Brillouin zone was sampled by the k-point mesh following the Monkhorst-Pack scheme,[61] with a reciprocal space resolution of $2\pi\times0.03$ Å^{-1}. On geometry optimization, both the shapes and internal structural parameters of pristine unit-cells were fully relaxed until the residual force on each atom is less than 0.01 eV/Å.

B. High-Throughput Settings

The purpose of this work is to identify the candidates of 2D semiconductors through large-scale screening of known materials, rather than to make the most accurate prediction of a specific material. To screen the novel 2D semiconductors, we used the VASPKIT package[62] as a high-throughput interface to pre-process the input files and post-process the data obtained by using VASP code. The overview of the screening process is in Fig. 1. First, VASPKIT generates three input files (POTCAR, KPOINTS, and INCAR) for a given structure file (POSCAR). Then the spin-polarized structure-relaxation was done to determine the magnetic ground state for each 2D material. If the candidate is non-magnetic, we next calculated the global band structure at the PBE level to determine the accurate positions of both conduction-band minimum (CBM) and valence-band maximum (VBM) in the reciprocal space. It is well known that the PBE functional is sufficiently accurate on band dispersion, but underestimates band gaps. The HSE06 can well describe narrow and middle-sized gap semiconductors whose valence electrons are not strongly localized.[57,63] As band structure calculations at HSE06 level is rather time-consuming, we have only performed the static HSE06 calculations on irreducible k-points including the positions of both CBM and VBM in order to get accurate band gap E_g values at the PBE-calculated lattice constants. If the candidate meets the energetic, thermodynamic, mechanical, dynamic and thermal stability criteria and bears a non-zero band gap, it could be a potential 2D semiconductor. Finally, we have further screened potential 2D semiconductors and heterostructures for water splitting according to the photocatalytic criteria which willl be discussed later. This screening algorithm is expected to be applicable to other fields, such as 2D thermoelectricity materials.

III. SCREENING CRITERIA

A. Thermodynamic Stability

Generally speaking, a stable material should have thermodynamic, mechanical, dynamic and thermal stabilities simultaneously. Thermodynamic stability measures the steadiness of a compound against its decomposition. Three physical quantities are commonly used to evaluate the thermodynamic stability of a free-standing 2D sheet, namely, the exfoliation energy, the energy convex hull and the formation energy. The exfoliation energy is the energy needed to exfoliate a monolayer from its bulk, an indication of the strength of interlayer bonds holding the layered bulk structure together. However, some 2D materials, such as borophene,[64] lack any layered bulk structure from which they can be exfoliated. The energy convex hull describes the competition between all phases with the same composition. Specifically, the phases lying above the convex hull have a tendency to decompose into the ground state compounds on the convex hull. The definition of energy convex hull, nevertheless, has the same problem as the exfoliation energy.[65,66] For example, the synthesis of 2D sheets by mechanical exfoliation implies that it is an endothermic process to break the interlayer bonds. This means that all 2D materials with respect to their corresponding bulk counterparts naturally fall above the convex hulls. The formation energy which is defined as the difference between a material and its pure elemental constituents in their ground states

$$\Delta E_f = E_{tot} - \sum n_\alpha \mu_\alpha, \tag{1}$$

where E_{tot} is the total energy of pristine 2D monolayer. n_α is the number of atoms of species α and μ_α is the atomic chemical potential of species α which is equal to the total energy of per atom in its most stable elemental phase. A more negative ΔE_f for a material means higher thermodynamic stability. However, to be thermodynamically stable, a material must not only have a negative formation energy not only with respect to the elemental ground states but also have a negative one with respect to all possible competing compound phases. In the present study we mainly focus on the high throughput computational screening of 2D semiconductors, and adopt the PBE-calculated formation energy as the thermodynamic stability criteria. PBE generally underestimate the formation energy of solids, especially for the layered materials, with an accuracy of only around 0.2 eV/atom on average.[67] We noted that the PBE-calculated forma-

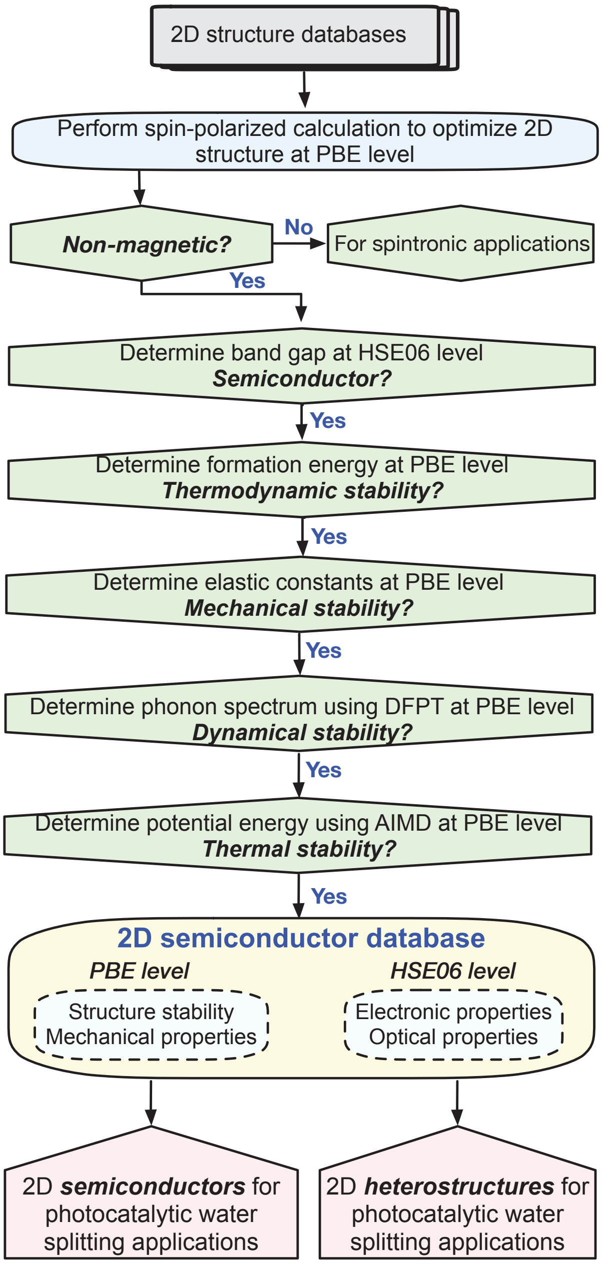

FIG. 1. (Color online) Schematic representation of the fundamental steps needed to find two-dimensional semiconductors.

tion energies of Si, Ge and Sn monolayer are higher than 0.6 eV/formula-unit (f.u.) but they have recently been synthesized or isolated by exfoliation.[25,26,28] In our high-throughput screening process, we used a threshold of 1.0 eV/f.u. as an upper bound on the thermodynamic stability for free-standing monolayers.

B. Mechanical Stability

The mechanical stability of a material describes its resistance to deformations or distortions in the presence of strain. For a 2D crystal in the linear elastic region, the stress $\sigma = (\sigma_1, \sigma_2, \sigma_6)$ response to external loading strain $\boldsymbol{\varepsilon} = (\varepsilon_1, \varepsilon_2, \varepsilon_6)$ follows the generalized Hooke's law and can be simplified in the Voigt notation,[68,69]

$$\begin{pmatrix} \sigma_1 \\ \sigma_2 \\ \sigma_3 \end{pmatrix} = \begin{pmatrix} \mathrm{C}_{11} & \mathrm{C}_{12} & \mathrm{C}_{16} \\ \mathrm{C}_{21} & \mathrm{C}_{22} & \mathrm{C}_{26} \\ \mathrm{C}_{61} & \mathrm{C}_{62} & \mathrm{C}_{66} \end{pmatrix} \cdot \begin{pmatrix} \varepsilon_1 \\ \varepsilon_2 \\ \varepsilon_6 \end{pmatrix},$$

where C_{ij} (i,j=1,2,6) is the in-plane stiffness tensor using the standard Voigt notation: 1-xx, 2-yy, and 6-xy. The C_{ij} can be obtained using the energy-strain method implemented into the VASPKIT code,[62] namely,

$$\begin{aligned} &E_{\text{elastic}}\left(E,\{\varepsilon_i\}\right) = E(S,\{\varepsilon_i\}) - E\left(S_0, 0\right) \\ &= \frac{S_0}{2}(C_{11}\varepsilon_1^2 + \mathrm{C}_{22}\varepsilon_2^2 + 2C_{12}\varepsilon_1\varepsilon_2 \\ &+2C_{16}\varepsilon_1\varepsilon_6 + 2C_{26}\varepsilon_2\varepsilon_6 + C_{66}\varepsilon_6^2). \end{aligned} \tag{2}$$

In the energy-strain method, the C_{ij} is equal to the second partial derivative of strain energy $E_{elastic}$ with respect to strain ε, and can be written as $\mathrm{C}_{ij} = (1/S_0)(\partial^2 E_{elastic}/\partial\varepsilon_i\partial\varepsilon_j)$, where S_0 is the equilibrium area of the system. Therefore, the unit of elastic stiffness constants for 2D materials is force per unit length (N/m). In order to calculate C_{ij}, the $E_{elastic}$ as a function of ε in the strain range -2% $\leqslant \varepsilon \leqslant$ 2% with an increment of 0.5% are investigated. The number of independent elastic constants is controlled by the symmetry of a 2D crystal. For instance, the hexagonal crystals have two but the oblique ones have six independent elastic constants. This number, together with the necessary and sufficient elastic stability conditions for different 2D lattice types are summarized in Fig. 2.[69,70]

C. Dynamic Stability

The dynamic stability reflects the structural tolerance of a system against small atomic displacements due tothermal motions. It can be determined by calculating the phonon dispersions of a material using either a finite displacement method[71] or density functional perturbation theory[72]. To be dynamically stable, a material allows no imaginary phonon spectra in its phonon dispersions. Shown in Fig. 3 (a) is the phonon spectra of hexagonal $\mathrm{MoS_2}$ monolayer. No imaginary modes appear, implying that is dynamically stable. Otherwise, the material will undergo reconstructive or martensitic phase transformations upon a slight lattice distortion. We derived phonon dispersions using the finite displacement approach implemented in the PHONOPY code.[73] The force constants were calculated using a supercell (20 Å × 20 Å) with atomic displacements of 0.01 Å along the lattice vectors.

It is worth mentioning that small negative spectra, *i.e.*, low imaginary frequency near the Γ point is often observed in the phonon spectra of 2D systems, as is the case for borophene monolayer [Fig. 3 (c)] which has been synthesized recently.[64] Such small imaginary frequencies could be an artifact of poor convergence due to limited supercell size, cutoff energy, or k-points; or they may reflect the actual lattice dynamical instability towards large wave undulations of 2D materials. It can possibly be eliminated by applying a small strain on the film or depositing the film onto a proper substrate.[64,74] Thus, a candidate is still considered to be dynamically stable even if a tiny imaginary frequency is present near the Γ point. We note that the phonon criterion is still a necessary but not sufficient condition to evince dynamic stability of a material. Since the phonon analysis deals only with small atomic displacements, it cannot capture phase transitions coupled with complex lattice reconstructions.[66]

D. Thermal Stability

Finally, the thermal stability of a material reflects its resistance to decomposition or reconstruction into lower energy structures at high temperatures, and can be evaluated by performing *ab-initio* molecular dynamics (AIMD) simulations over a long time and wide range of temperatures. To verify the dynamic stability of the proposed 2D materials, we employed AIMD simulations of a 10 Å × 10 Å supercell model at a temperature of 400 K. The time step and time duration are set to 1.0 fs and 60 ps, respectively. A Nosé-Hoover thermostat was used to control the temperature.[75] To be dynamically stable, its potential energy should remain roughly constant during the AIMD simulation. For comparative purpose, we found that the calculated potential energy of BP ($Pmma$) fluctuates around the equilibrium state as a function of time [Fig. 4 (a)], indicating a good thermal stability. In contrast, the potential energy of $\mathrm{MgI_2}$ ($P\bar{3}m1$) decreases over time, reflecting an irreversible change in structure which lowers the formation energy. The snapshot of its atomic configuration at the end of the simulation further shows that this material is drastically distorted and is unlikely to be fabricated in the free-standing forms.

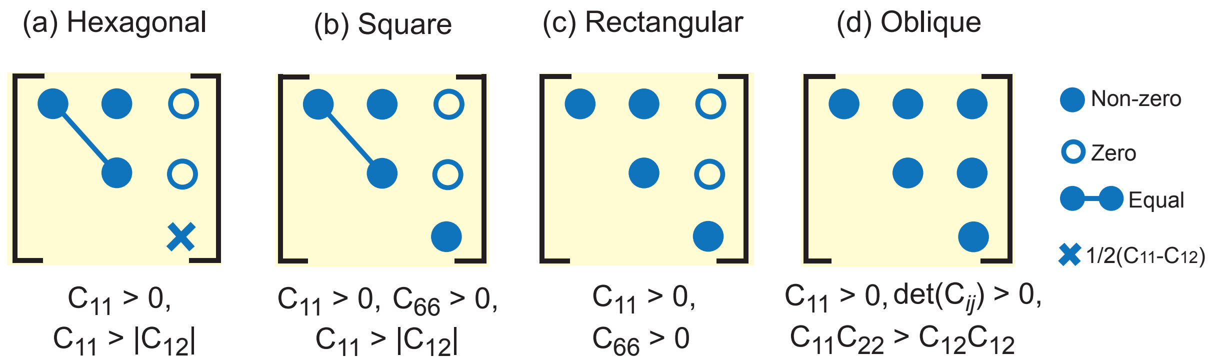

FIG. 2. Classification of crystal systems, independent elastic constants, elastic stability conditions for 2D materials.

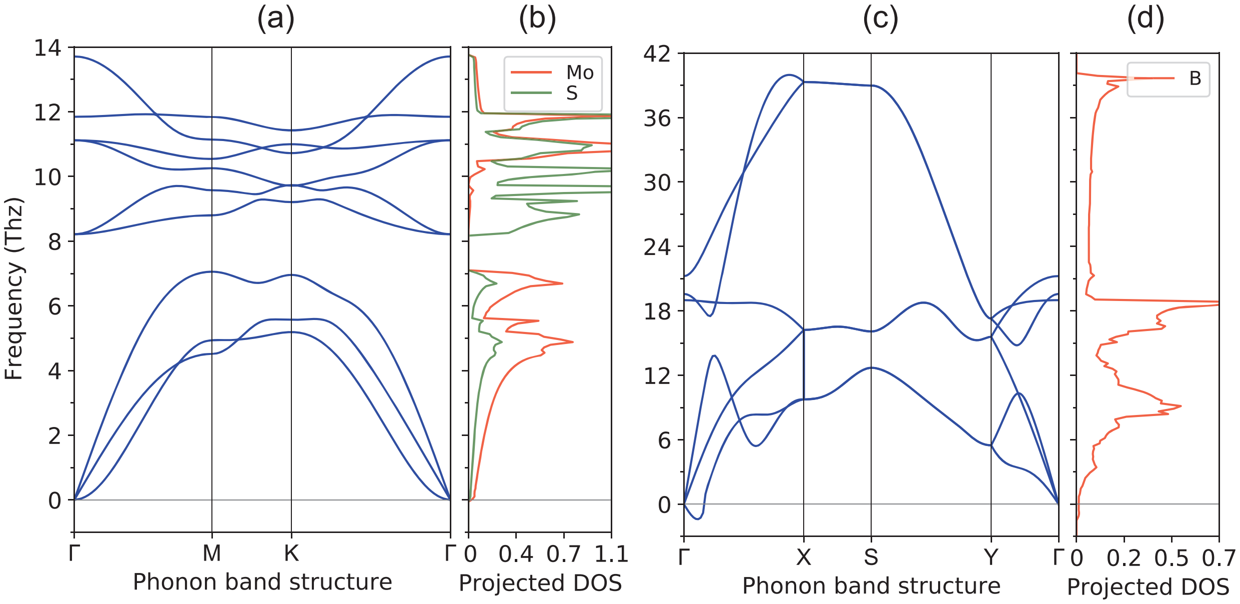

FIG. 3. (Color online) Calculated (a) and (c) phonon dispersion curves, projected density of states (b) and (d) for H-MoS$_2$ and borophene sheet respectively.

E. Semiconductor Screening

For nonmagnetic semiconductors, the Kohn-Sham (KS) band gap E_g is defined as the difference between the eigenvalues of CBM and VBM. That is,

$$E_g = \epsilon_{\mathrm{CBM}} - \epsilon_{\mathrm{VBM}}, \tag{3}$$

where ϵ_{CBM} and ϵ_{VBM} are the KS eigenvalues of CBM and VBM respectively. It is well known that PBE severely underestimates the band gap of semiconductors because of the lack of derivative discontinuity of the functional with respect to the number of electrons and the lack of clear physical meaning of the unoccupied orbitals. But PBR yields similar band dispersion curves to the hybrid DFT result. There are five typical 2D Bravais lattices, namely, hexagonal, square, rectangular, centered rectangular, and oblique respectively. The Ball-and-stick models, Brillouin zones and suggested k-paths for the Bravais lattices adopted in our high-throughput calculations are presented in Fig. 5 and Table I.

IV. RESULTS AND DISCUSSIONS

Based on the above criteria, we have screened 74 direct- and 184 indirect-gap 2D nonmagnetic semiconductors from near 1000 2D monolayers. By analyzing the occurrence frequency of each element in the screened 2D semiconductors shown in Fig. 6, it is found that the most abundant candidates are oxides, followed by sul-

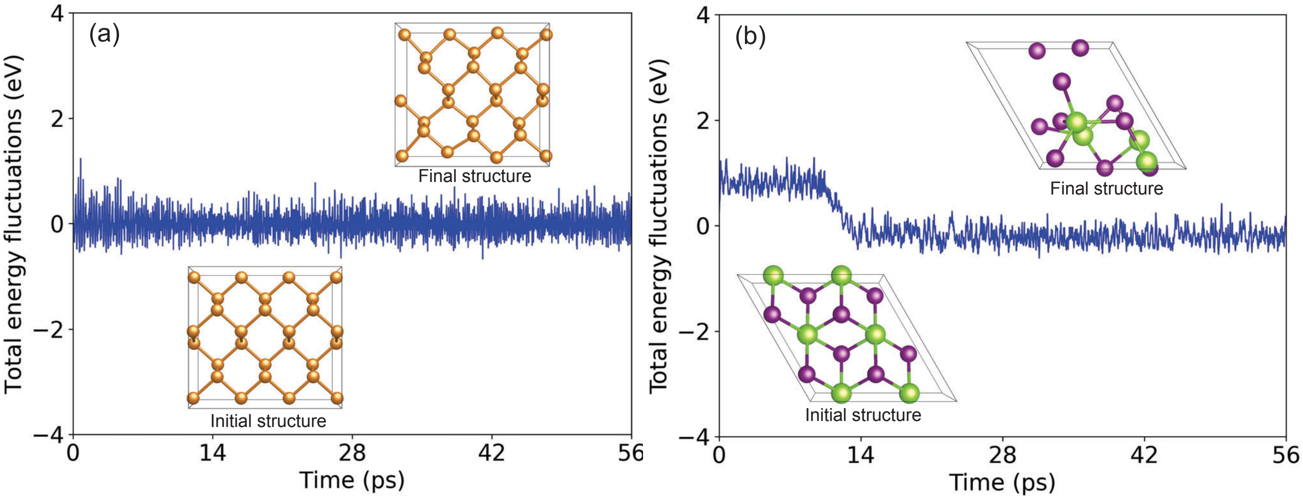

FIG. 4. (Color online) Total potential energy fluctuations of (a) BP ($Pmma$) and (b) MgI_2 ($P\bar{3}m1$) during AIMD simulations at 400 K. The inset shows the snapshots at the begin and end of simulation. The results show that MgI_2 tends to reconstruct into lower energy structure and is unlikely to be realized experimentally in the freestanding forms.

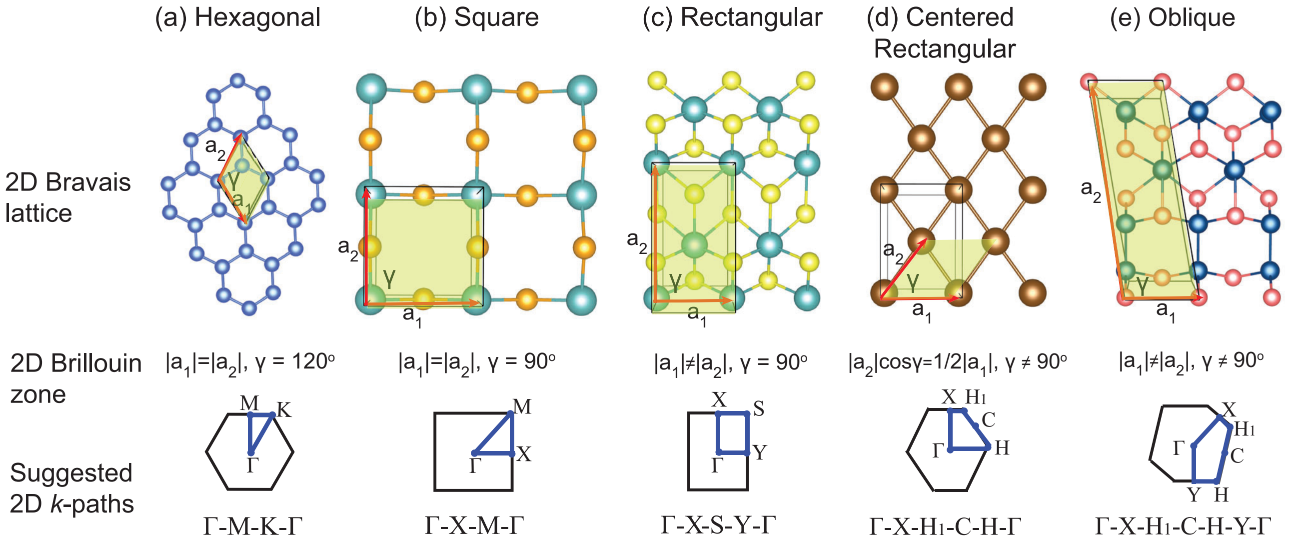

FIG. 5. (Color online) Overview of the five 2D Bravais lattices and corresponding Brillouin zones. The suggested k-paths for band structure are indicated in blue line. The primitive unit cell is indicated in green box.

1/3

fides, selenides and halides. Meanwhile, the cations appear to favor heavy metal elements such as Pd, Zr, Hf and Pb. The classifications of these candidates according to the relative frequencies of lattice type, stoichiometry and space group of the crystals are further summarized in Figs. 7(a)-(c), respectively. Note that the lattice types of 2D semiconductors are dominated by rectangular (43.4%) and hexagonal (40.3%), and the least abundant are square (16.3 %). Most of them are binary compounds predominantly bearing by AB_2 structures. Moreover, the space groups of these candidates are mainly $P2_1/m$ and $P\bar{3}m1$. It is noteworthy that TMDs are one of the most interesting families in the AB_2 layered compounds and display a wide range of important properties. The TMD monolayers have three phases, namely, 2H ($P\bar{6}m2$), 1T ($P\bar{3}m1$) and 1T' ($P2_1/m$), respectively. Previous theoretical studies have predicted that around 50 different transition-metal oxides (TMOs) and TMDs can remain stable as either 2H and/or 1T free-standing structures,[76,77] even though part of these potential MX_2 compounds are absent in their bulk counterparts. For the sake of completeness, we also revis-

TABLE I. Fractional coordinates of the specific points in reciprocal space for the four nonequivalent two-dimensional Bravais lattices.

Bravais Lattice	Label and coordinates of specific points	Bravais Lattice	Label and coordinates of specific points
Square	$\mathbf{\Gamma}$ (0, 0)	Oblique	$\mathbf{\Gamma}$ (0, 0)
	X (1/2, 0)		**X** (1/2, 0)
	M (1/2, 1/2)		**Y** (0, 1/2)
Hexagonal	$\mathbf{\Gamma}$ (0, 0)	Oblique	**C** (1/2, 1/2)
	K (1/3, 1/3)		**H** (η, 1-ν)[a]
	M (1/2, 0)		$\mathbf{H}_1$ (1-η, ν)[a]
Rectangular	$\mathbf{\Gamma}$ (0, 0)	Rectangular	**X** (1/2, 0)
	Y (0, 1/2)		**S** (1/2, 1/2)

[a] $\eta = \frac{1-acos\gamma/b}{2sin^2\gamma}$, $\nu = \frac{1}{2} - \frac{\eta bcos\gamma}{a}$ and $\gamma < 90°$.

ited the stability and electronic structure of TMOs and TMDs with three possible phases (2H, 1T and 1T' respectively). We find that the band gap of these semiconducting candidates is mainly concentrated between 1.0 and 3.0 eV. The PBE-calculated lattice constants, formation energy, Young's modulus, Poisson's ratio, scanning tunnel microscopy, anisotropic effective mass, as well as the HSE06-calculated band gap, ionization energy and electron affinity for each candidate are listed in the Supplemental Material.

A. Mechanical Properties

The mechanical properties of a single-crystal are generally anisotropict. The Voigt-Reuss-Hill (VRH) approximation,[78,79] is a useful scheme by which one can calculate isotropic polycrystalline elastic moduli in terms of the anisotropic single-crystal elastic constants. We present the VRH averaged bulk and shear moduli of binary 2D semiconductors as a function of the constituent elements in Fig. 8. One can find that oxides have the largest bulk modulus, followed by sulfides and then selenides. As expected, the shear modulus indicates positive correlations with bulk modulus. Next we compare our predicted data with available experimental or theoretical reports. Up until now, several monolayers have been successfully exfoliated or synthesized, including graphene (P6/mmm),[1] BP (Pmna),[14,19,20] borophene (Cmmm),[64] BN ($P\overline{6}m2$),[21,80] MoS_2 ($P\overline{6}m2$),[16] TiS_3 ($P2_1/m$)[81]. We summarize the calculated in-plane elastic stiffness constants, the minimum and maximum of Youngs's modulus, shear modulus and Poisson's ratio for these systems in Table II. One can find that our predictions are in good agreement with the available published data. For example, the PBE-calculated Young's modulus and Poisson's ratio of graphene are 339 N/m and 0.17, in excellent agreement with the available values of 340 N/m and 0.186,[82,83] respectively. To investigate the anisotropic mechanical properties of 2D materials, we also calculated the orientation-dependent Young's moduli $Y(\theta)$, Poisson's ratio $\nu(\theta)$ and shear modulus $G(\theta)$ using the following formulae,[84,85]

$$\begin{aligned} 1/E(\theta) = S_{11}c^4 + S_{22}s^4 + 2S_{16}c^3s \\ +2S_{26}cs^3 + (S_{66} + 2S_{12})\, c^2s^2 \end{aligned}, \tag{4}$$

$$\begin{aligned} \nu(\theta)/E(\theta) = (S_{66} - S_{11} - S_{22})\, c^2s^2 \\ -S_{12}\left(c^4 + s^4\right) + (S_{26} - S_{16})\left(cs^3 - c^3s\right) \end{aligned}, \tag{5}$$

and

$$\begin{aligned} 1/4G(\theta) = (S_{11} + S_{22} - 2S_{12})\, c^2s^2 + \\ S_{66}\left(c^2 - s^2\right)^2/4 - (S_{16} - S_{26})\left(c^3s - cs^3\right) \end{aligned}, \tag{6}$$

where $s = sin(\theta)$, $c = cos(\theta)$, and $\theta \in [0, 2\pi]$ is the angle with respect to the $+x$ axis. $S_{ij} = C_{ij}^{-1}$ are elastic compliance constants. As an example, It is found in Fig. 9 that the mechanical properties of a BP monolayer shows a strong anisotropy. It is expected that all but hexagonal 2D bravais lattices have the anisotropic mechanical properties.

Thermodynamic stability sets limits on the energy and the range of Poisson's ratio is allowed to be from -1.0 to 0.5. Most materials have a positive Poisson's ratio, shrinking (expanding) longitudinally after being stretched (compressed) laterally. We do find a few materials with a negative Poisson's ratio (NPR), also called auxetic materials. The NPR behavior is mainly attributed to some special re-entrant or hinged geometric structures regardless of the chemical composition and electronic structure of a material. The NPR materials exhibit fascinating mechanical properties, such as superior toughness, higher indentation resistance, larger impact resistance, stronger sound absorption, and better crack propagation resistance.[89] These excellent properties offers enormous potential in many important applications, such as automotive, aerospace, marine, and other industrial fields.[90,91] Recently, the auxetic effect has been reported in a number of 2D materials. In addition to monolayer phosphorus and arsenic allotrope reported in pre-

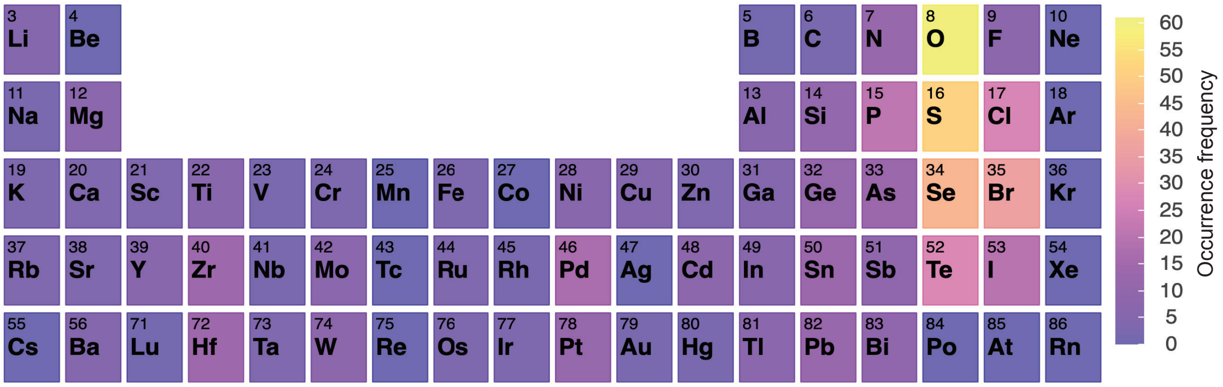

FIG. 6. (Color online) Heat map of the occurrence frequency of each element in the screened 2D semiconductors.

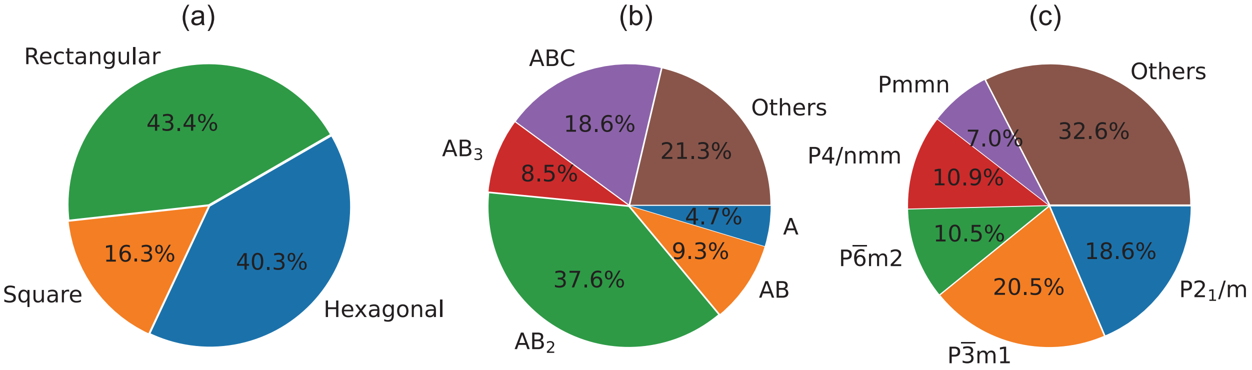

FIG. 7. (Color online) Classification of the screened 2D semiconductors in term of (a) lattice type, (b) stoichiometry and (c) symmetry.

vious studies,[92–94] we also screened some other 2D semiconductors with large NPR values, including As_2SO_6 (-0.392), SiP_2 (-0.320), BaIF (-0.256), GeSe (-0.228), SnS (-0.189) and SbSeI (-0.166). Among them, BaIF is the only one persisting the NPR in all crystal directions.

B. Electronic Properties

Beside the band structure, the projected band structure is also provided illustrate the contributions of different atomic orbitals in energy and momentum space, offering a chemist's perspective of the electronic structure. As examples, the element-resolved and orbital-projected band structures and the corresponding density of states (DOS) of MoS_2 and graphene monolayers are depicted in Fig. 11. To gain more insight into the topological characterization of band dispersions near Fermi energy, we calculated the global band structures of both VBM and CBM for each candidate at the PBE level. The global band structures of InN ($P\overline{6}m2$) and AgI (P4/nmm) are illustrated in Fig. 12. In addition, the orientation-dependent effective mass $m^*(\theta)$ of both holes and electrons can be further obtained from the global band structures, with the aim of analyzing the anisotropic band dispersions. The PBE-calculated 2D polar representation curves for BP, MoS_2 and TiS_3 are presented in Fig. 14 for illustration purpose. One can find that the effective masses of all representative semiconductors are highly anisotropic, especially for BP and TiS_3. The calculated m^* along Γ-X and Γ-Y are 0.32 (1.52) m_0 and 1.06 (0.38) m_0 for hole (electron) in TiS_3 monolayer, in good agreement with previous results, 0.32 (1.47) m_0 and 0.98 (0.41) m_0.[95] By comparison, the effective mass of hole (electron) in MoS_2 slightly increases from 0.54 (0.44) m_0 along K-Γ to 0.61 (0.47) m_0 along K-M due to the higher hexagonal symmetry. We define the anisotropy ratios of effective masses, $\gamma_h = m_h^{max}/m_h^{min}$ for hole and $\gamma_e = m_e^{max}/m_e^{min}$ for electron carriers. The calculated γ_h (γ_e) is 1.25 (1.14) for MoS_2, 3.18 (3.66) for TiS_3 and 128.67 (6.80) for BP.

To gain more insights into the band-gap variations of compounds, in Fig. 10 we show the HSE06 predicted band gap (E_g) of binary 2D semiconductors as a function of the electronegativity difference between two constituent elements. The introduction of electronegativity difference here is to roughly evaluate the ionic character of the chemical bond formed between different elements.

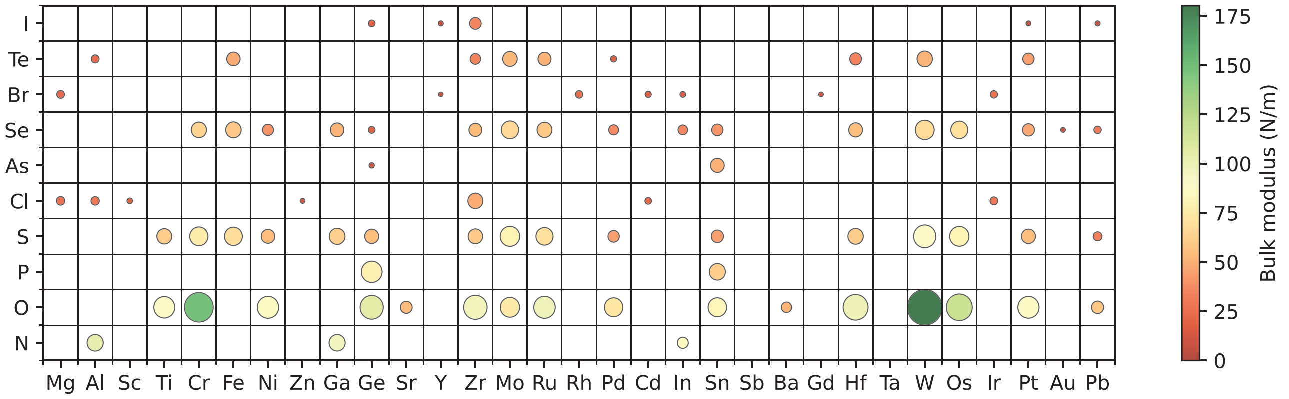

FIG. 8. (Color online) Bulk and shear modulus of binary 2D semiconductors as a function of the constituent elements within Voigt-Reuss-Hill (VRH) approximation. The circle radius represents the magnitude of shear modulus.

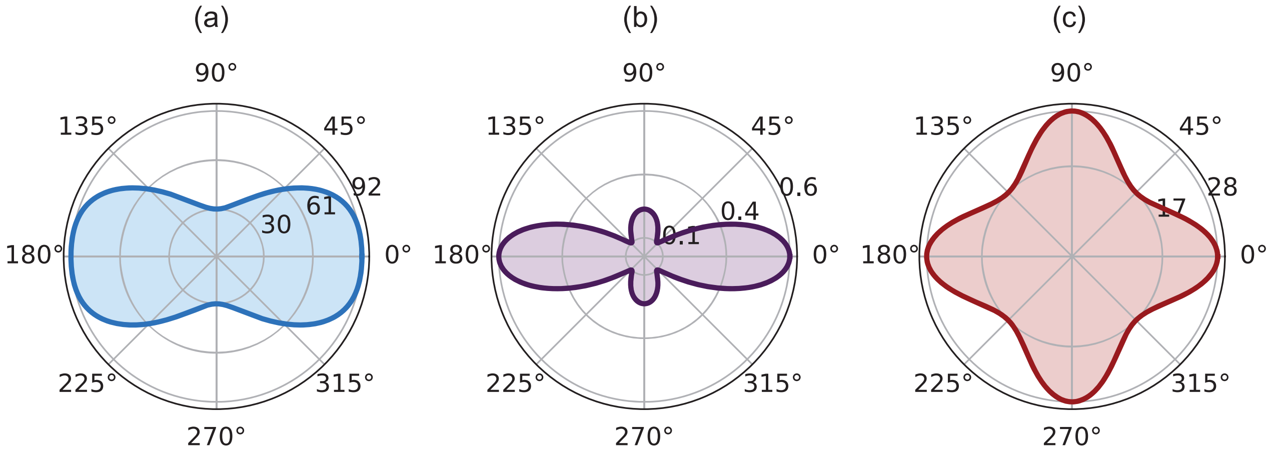

FIG. 9. (Color online) Calculated orientation-dependent (a) Youngs's modulus $E(\theta)$, (b) Poisson's ratio $\nu(\theta)$ and (c) shear modulus $G(\theta)$ for BP respectively.

A larger difference in electronegativity implies a stronger ionic character. Overall, it is found that a compound with a stronger ionic bond tends to own a larger band gap value. Nevertheless, there are some exceptional cases in which small gaps come along with large electronegativity difference, such as CrO_2, $ZrCl_2$ and $HfSe_3$. In the electronic and optoelectronic devices applications, not only the band gap, but also the absolute position of the band edges relative to vacuum, including ionization energy (I) and electron affinity (A) and work function (ϕ) are important parameters. I is the minimum energy needed to remove an electron from the highest occupied state to the vacuum, i.e. at V_{vac}, I=$V_{\mathrm{vac}}-\varepsilon_{\mathrm{VBM}}$. A is the negative of the energy change when adding an electron to the lowest unoccupied state, A=$V_{\mathrm{vac}}-\varepsilon_{\mathrm{CBM}}$. Clearly, the absolute positions VBM and CBM with respect to V_{vac} are the negatives of I and A, respectively. The work function (ϕ) is defined as the minimal energy needed to remove an electron originally at the Fermi level (E_F) deep inside the material to just outside its surface, namely, ϕ=$V_{\mathrm{vac}}-E_F$. In semiconductors, ϕ varies with the position of the E_F because E_F is strongly sensitive to the preparation condition of the sample in the measurement which determines to a large extent concentration of various intrinsic and extrinsic defects. Figure 13 provides a schematic illustration of different quantities involved. In the KS-DFT scheme, the calculation of V_{vac} is straightforward as it equals to the asymptotic value of the planar-averaged Hartree potential in the vacuum region, as illustrated in Fig. 13. The band edges of several widely studied 2D semiconductors, together with available theoretical data in literature, are listed in Table 18. One can find that the HSE06 calculated E_g, I and A of the representative systems are in good agreement with previous reports.[16,21,96,97]

TABLE II. PBE-calculated in-plane elastic stiffness constants, Youngs's modulus $Y(\theta)$, shear modulus $G(\theta)$ (in units of N/m), and Poisson's ratio $\nu(\theta)$. For comparison purposes, the available theoretical or experimental values from the previous literature are also shown.

	C_{11}		C_{22}		C_{12}		$E(\varphi)$		$G(\varphi)$		$\nu(\varphi)$	
Systems	Calc.	Refs.	Calc.	Refs.	Calc.	Refs.	Max	Min	Max	Min	Max	Min
Graphene	349	342 [86]	349	342 [86]	60	-	339	339	144	144	0.17	0.17
BP	106	105 [87]	34	26 [87]	22	18 [87]	92	29	28	17	0.63	0.08
BN	292	289 [86]	292	289 [86]	64	-	277	277	114	114	0.22	0.22
MoS_2	131	124 [88]	131	124 [88]	33	-	122	122	49	49	0.26	0.26
TiS_3	88	83 [88]	137	134 [88]	14	-	137	71	47	25	0.42	0.10

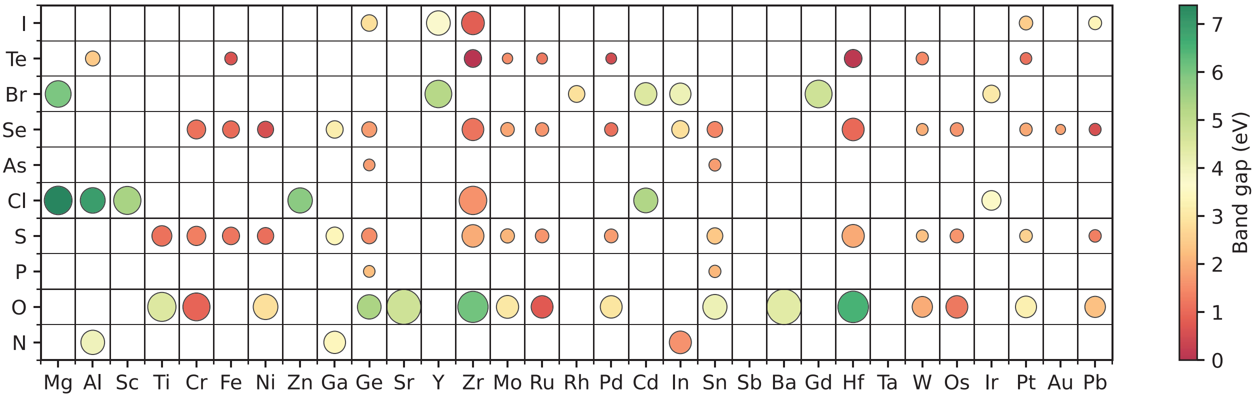

FIG. 10. (Color online) HSE06 calculated band gap of binary 2D semiconductors as a function of the electronegativity difference between two constituent elements. The circle radius indicates the electronegativity difference.

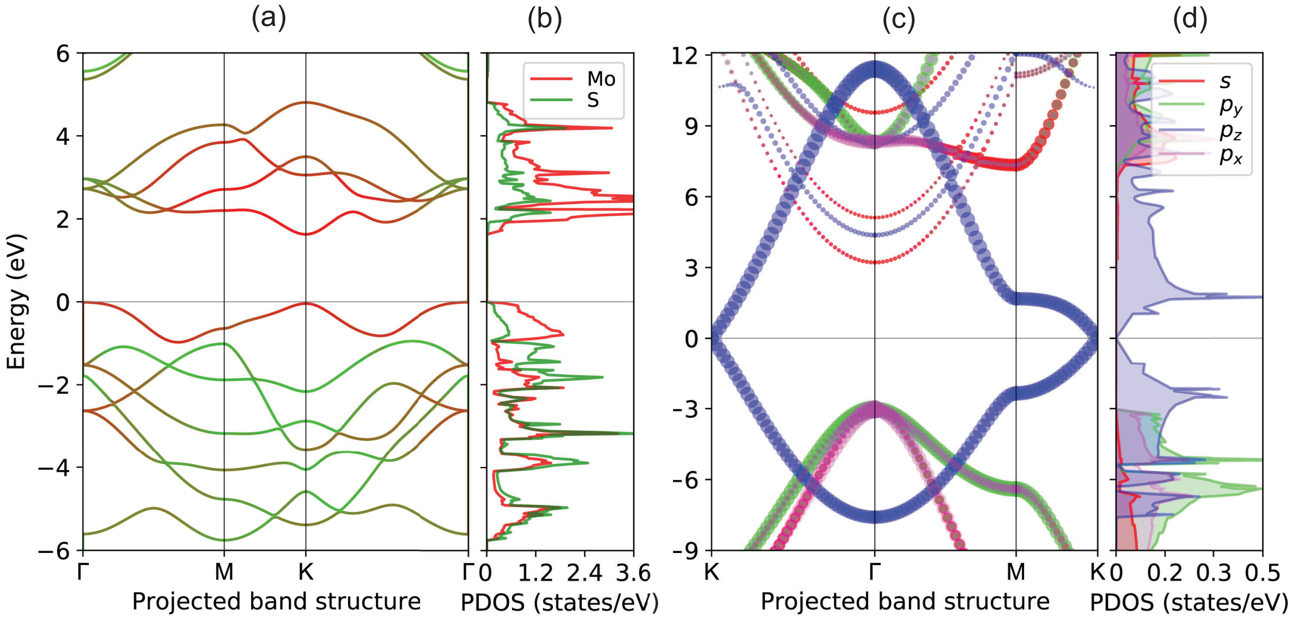

FIG. 11. (Color online) Projected band structure (left panel) and density of states (right panel) of (a) MoS_2 and (b) graphene monolayers. The Fermi energy is set to zero eV.

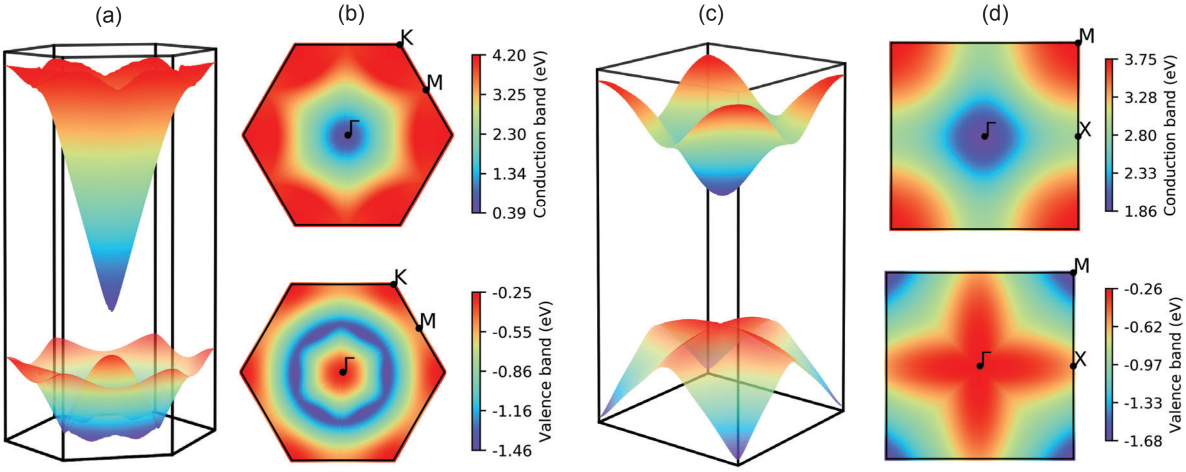

FIG. 12. (Color online) PBE calculated global band structure of (a) InN ($P\overline{6}m2$) and (b) AgI (P4/nmm).

TABLE III. HSE06-calculated band gap E_g, ionization energy I and electron affinity A. For comparison purposes, the available theoretical values from the previous literature are also shown.

Material	Band gap (eV)		Ionization energy (eV)		Electron affinity (eV)	
	Our work	Literature	Our work	Literature	Our work	Literature
BP	1.57	1.52 [98]	5.46	5.43 [98]	3.89	3.91 [98]
BN	5.71	5.68 [99]	6.60	6.56 [99]	0.89	0.88 [99]
MoS_2	2.18	2.15 [99]	6.38	6.33 [99]	4.20	4.18 [99]
WSe_2	2.04	1.98 [100]	5.49	5.82 [100]	3.45	3.84 [100]
TiS_3	1.15	1.06 [101]	5.87	5.34 [101]	4.72	4.28 [101]

C. Optical Properties

The macroscopic dielectric function of 2D materials cannot be well-defined with the layer thickness $d \to 0$. This is because the calculated dielectric function of an artificial 3D periodic system is affected by the length L of the vacuum region in the standard DFT calculations. To avoid the thickness problem, an L-independent optical conductivity $\sigma_{2D}(\omega)$ is used to characterize the optical properties of 2D sheets,[102,103]

$$\sigma_{ij}(\omega) = \varepsilon_0 \omega L \left[\varepsilon_{ij}(\omega) - \delta_{ij}\right], \tag{7}$$

where $\varepsilon(\omega)$ is frequency-dependent complex dielectric function calculated in the framework of the independent-quasiparticle approximation[104], ε_0 is the permittivity of vacuum, ω is the frequency of incident wave, and L is the slab thickness in the simulation cell. In the present study we consider only the in-plane component $\varepsilon(\omega)$ of the dielectric tensor, *i.e.*, only light polarization perpendicular to the sheet normal has been taken into account. The normalized reflectance $R(\omega)$, the transmittance $T(\omega)$, and the absorbance $A(\omega)$ can be obtained from the following equation:[102,103]

$$\begin{aligned} R &= \left|\frac{\tilde{\sigma}/2}{1+\tilde{\sigma}/2}\right|^2 \\ T &= \frac{1}{|1+\tilde{\sigma}/2|^2} \\ A &= \frac{\mathrm{Re}\,\tilde{\sigma}}{|1+\tilde{\sigma}/2|^2} \end{aligned} \tag{8}$$

where $\tilde{\sigma}(\omega) = \sigma_{2\mathrm{D}}(\omega)/\varepsilon_0 c$ is the normalized conductivity (c is the speed of light). We present the linear optical properties of graphene in Fig. 15 as an illustrated example.

D. Scanning Tunneling Microscope Simulations

STM can not only characterize the atomic structure of material surfaces, but also can provide direct local insight into the electronic structure.[105] Thus, the simulated STM image has been obtained for each candidate based on the Tersoff-Hamann approach.[106] In this model the calculated tunneling current I which depends on the tip position $\mathbf{r}$ and the applied voltage V, is proportional to the integrated local density of states (LDOS)

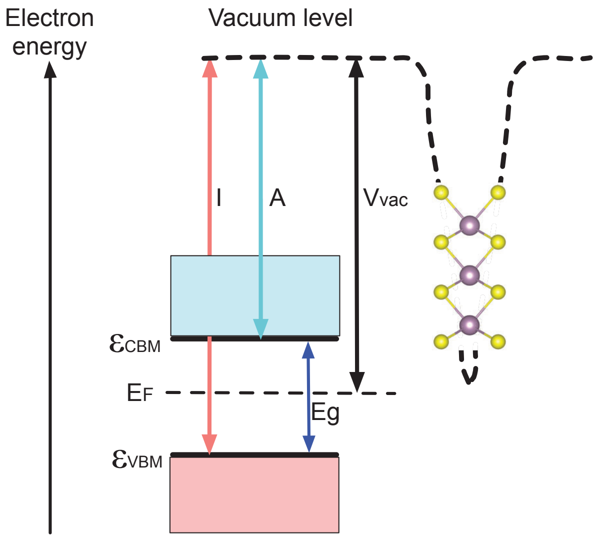

FIG. 13. (Color online) Schematic energy diagram of a semiconductor. The ionization energy I, electron affinity A and work function ϕ defined as the energies of VBM, CBM and Fermi level E_F with respect to the vacuum level $V_{\rm vac}$, respectively.

$$I(\mathbf{r}, V) \propto \int_{\epsilon_F}^{\epsilon_F+eV} \sum_{kn} w_{\mathbf{k}} \left|\Psi_{\mathbf{k}n}(\mathbf{r})\right|^2 \delta\left(\epsilon - \epsilon_{\mathbf{k}n}\right) d\epsilon, \quad (9)$$

where V is the bias voltage, $w_{\mathbf{k}}$ is the k-point weight, $\Psi_{\mathbf{k}n}(\mathbf{r})$ and $\epsilon_{\mathbf{k}n}$ are the wave function and eigenvalue at the wave-vector $\mathbf{k}$ with band index n, and ϵ_F is the Fermi-energy. To simulate STM images, we integrated the LDOS from 0.5 eV below the VBM up to 0.5 eV above the CBM. We chose the tunneling tip of 1.0 Å and 2.0 Å above the upper surface of 2D semiconductors during the simulations, respectively. Constant current topographs are approximated by constant charge density isosurfaces. In Figs. 16(a)-(c), we give the calculated STM images of graphene, BP and h-BN with examples. Clearly, we observe that the patterns in the computational and experimental STM images are very similar.[107–109]

E. van der Waals Heterojunctions

According to the alignments of the CBM and VBM in the constituent layers, heterojunctions can be classified into three types: type I (straddling gap), type II (staggered gap), or type III (broken gap), as illustrated in Fig. 19(a), respectively. In type I heterojunctions, both VBM and CBM of two independent component semiconductors are located at the same side of the heterointerface. This is beneficial for spatially confining electrons and holes so that efficient recombination can be achievable, rendering them potential applications in optoelectronic devices such as lightemitting diodes (LEDs).[110] In type II heterojunctions, the CBM and VBM are located in different components with electrons accumulating in the layer with the lower CBM and holes accumulating in the other layer with the higher VBM. Different from type I band alignment, the separation of electrons and holes to different layers can increase carrier lifetime, which is desirable for photocatalysis and unipolar electronic device applications including photovoltaics and photodetection applications[44,111–114] In type III heterojunctions, the VBM of one semiconductor is higher than the CBM of the other, making the whole system overall heterojunction metallic. Such a property could have great potential in tunnel field-effect transistors and wavelength photodetectors.[115,116]

The high-throughput design of vdWHs has gained significant attention because vdWHs have unique physical properties and potential applications mentioned above. Rasmussen *et al.* theoretically predicted the band alignments of 51 semiconducting TMDs and TMOs monolayers using GW0 calculations.[77] Latterly, äzçelik *et al.* established a periodic table of band alignments cover about 900 vdWHs by performing hybrid functional calculations.[99] Nevertheless, these studies focused only on groups IV, III-V and V elemental and/or compound monolayers, TMDs and transition-metal trichalcogenides (TMTs). To have a thorough search, we have extended the HSE06 calculated periodic table of heterostructure types formed by any two of the 200 screened semiconductors. The flowchart for the computational design of vdWHs is illustrated in Fig. 19(b). To determine the band alignment type when A and B monolayers were stacked together, we first compared the absolute positions of VBM and CBM by aligning the vacuum level of two composed monolayers to 0 eV based on Anderson's rule[117]. The band gap of vdWH was then estimated by the difference between the lower CBM energy and the higher VBM energy of two monolayers. The resulting vdWH is type I if both the higher VBM and lower CBM are located at the same layer. Otherwise, it belongs to type II or type III. Next the II and III can be separated by the band gap of vdWH being larger than zero or not.

Considering that the dimension table of complete vdWHs type is very huge (around 20000), we only list the periodic table of vdWHs for about 2000 hexagonal systems in Fig. 18. Our results show that the hexagonal vdWHs are dominated by type II (44.6%) and type I (43.8%), and the least abundant are type III (11.6 %). In contrast, the complete periodic table provided in the Supplemental Material shows that half of 20000 vdWHs are type I (46.0%), followed by type II (39.1%) and type II (14.9%). One can find that the vdWHs composed of light elements are dominated by type I and II (near the upper left corner); while the vdWHs composed of heavy elements tends to form type III heterojunctions. This is mainly because the 2D semiconductors composed of heavy elements have higher ionization energy than those composed of light ones. Overall, the agreement between our calculated results and the corresponding

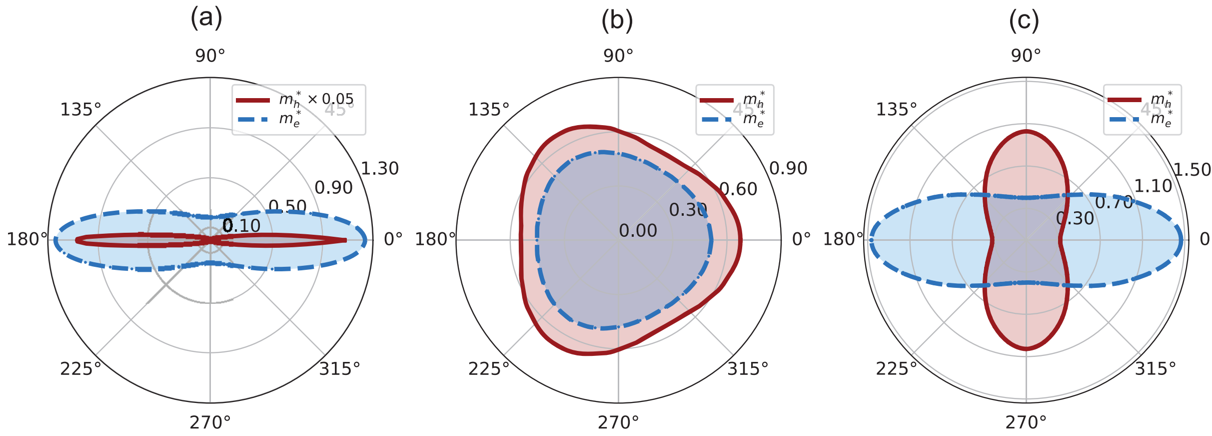

FIG. 14. (Color online) PBE calculated orientation-dependent effective masses (in units of electron mass m_0) of (a) BP, (b) MoS_2 and (c) TiS_3 monolayers. The red and blue lines indicate the fitted effective mass curves of hole and electron carriers, respectively.

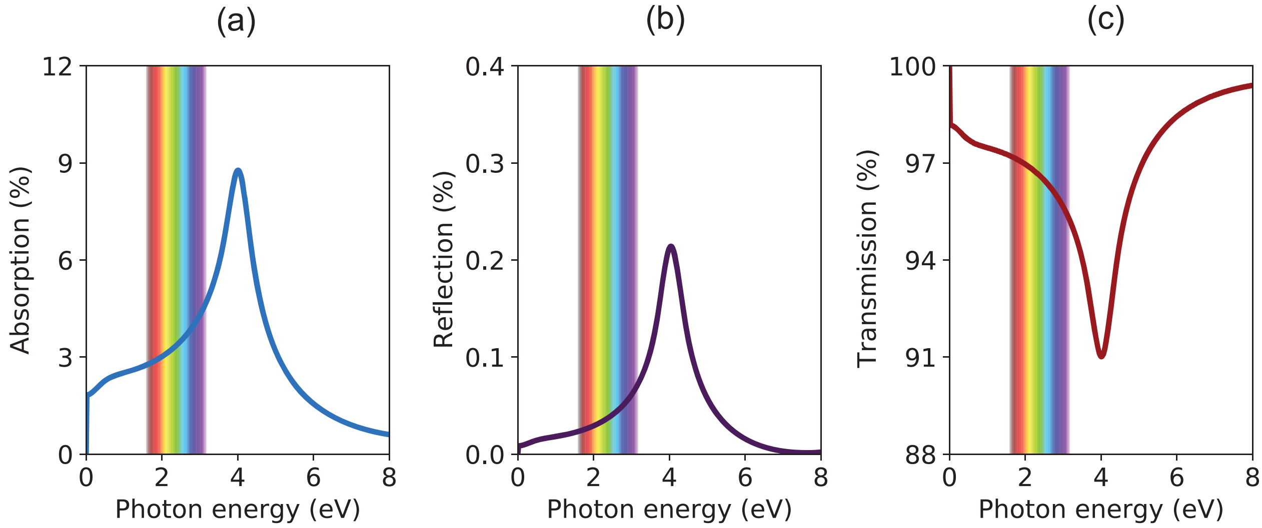

FIG. 15. (Color online) Frequency dependence of (a) absorbance, (b) reflectance and (c) transmittance for graphene.

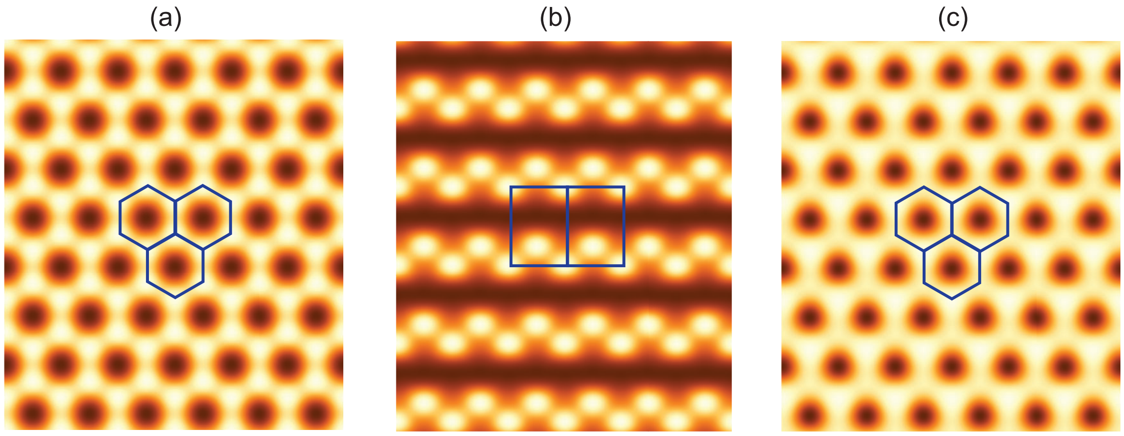

FIG. 16. (Color online) Simulated STM image of (a) graphene, (b) BP and (c) *h*-BN respectively.

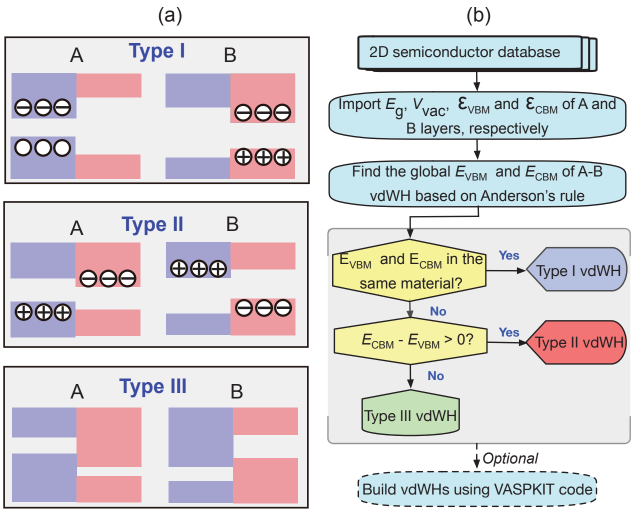

FIG. 17. (Color online) (a) Schematic illustrations of the three types of semiconductor heterojunctions based on their energy band alignments: type I (straddling gap), type II (staggered gap), and type III (broken gap) heterojunctions. (b) flowchart for the computational design of vdWHs.

experimental values is very good. For examples, ultrafast charge transfer was observed in MoS_2/WS_2 type II heterojunction,[111] and moiré-trapped valley excitons was observed in $MoSe_2/WSe_2$ type II heterojunction,[118] We believe the predicted periodic table of vdWHs would provide a useful guidance for experimentalists to design suitable vdWHs with desired band alignment type.

To validate the band-alignment description with the predictions from Anderson's rule, three representative heterojunctions with relatively small lattice, $ZrO_2/MoSe_2$, $WSe_2/MoSe_2$ and $NiS_2/ZrCl_2$ were chosen to revisit their band alignments by performing HSE06 calculations. Their layer-resolved band structures are shown in Fig. 19. One can find that the band alignments predicted using Anderson's rule is similar to the DFT results. As expected, no significant interlayer hybridization between the two components of vdWHs is found. It needs to be emphasized that the Anderson's rule-based approach is a rough estimation. It may work only qualitatively as plays an important role in determining the band structures of 2D materials.[38,39,119,120]

Part of the interlayer coupling arises from the electronegativity difference between the two, which might cause band shifts and band gap variations in vdWHs. The magnitude of interlayer coupling dependent on layer-thickness, interlayer distance, stacking order, interlayer twist angle, constituent elements, the symmetry of two components, *etc.* Furthermore, for the lattice-mismatched vdWHs, the internal stress between the constituent layers is more likely to modify their band structures in addition to direct interlayer coupling. Thus, it is expected that the vdWH type can vary due to the interlayer coupling and internal stress if the difference of absolute band extrema of two components is not significant. Nevertheless, the effect of interlayer coupling on the electronic structures of vdWHs is rather complicated and beyond the scope of the present work.

F. 2D Semiconductors and Heterojunctions for Water Splitting Photocatalysts

Photocatalytic water splitting has been attracting tremendous attention as an energy-efficient and environmental protective route to produce hydrogen. 2D materials possess inherent advantages to improve photocatalytic performance for water splitting. To be a promising candidate for water splitting, a semiconductor should meet three basic requirements:[45,121] (i) being chemically stable and insoluble in water; (ii) band gap being larger than the free energy of water splitting of 1.23 eV and smaller than 3 eV to enhance solar absorption; and (iii) band edge position crossing the redox potentials of water,[122] *i.e.*,, the CBM being higher than the reduction potential of H^+/H_2 (-4.44 eV at pH = 0) and the VBM being lower than the oxidation potential (O_2/H_2) (-5.67 eV at pH = 0). Moreover, the redox potentials is influenced by the pH value in the water splitting reaction. Specifically, the pH-dependent reduction potential for H^+/H_2 and oxidation potential for O_2/H_2 are $E^{\rm red}_{\rm H^+}/{\rm H_2} = -4.44 + {\rm pH} \times 0.059$ eV and $E^{\rm ox}_{\rm O_2/H_2O} = -5.67 + {\rm pH} \times 0.059$ eV respectively.

On the basis of above-mentioned criteria (ii) and (iii), we have extended the photocatalysis screening procedure to our 2D semiconductor database. We obtained 53 kinds of monolayers possessing band edge positions which meet the requirement for photocatalytic water splitting at a certain pH value within 0-7, as shown in Fig. 20. These results include the extensively studied 2D semiconductors. For examples, recent experimental or computational studies have revealed that graphene-like g-C_3N_4,[123] C_2N,[124] MoS_2,[125] BP,[126] $PdSeO_3$,[127] SiP_2,[128] Bi_2Te_2S and Bi_2Te_2Se[129] are potential candidates for photocatalytic water splitting. Besides the previously reported monolayer materials, we have also screened around 40 novel monolayer semiconductors with good structural stability and proper band edge positions. Among them, there are 17 potential candidates being applicable to a wide range of pH value from 0 to 7. However, it should be emphasized here that the presence of appropriate band edge positions cannot guarantee an effective photocatalyst for overall water-splitting. The chemical stability of these candidates in exposure to water and air were not considered in our high-throughput screening calculations. Furthermore, the fast recombination of photoinduced carriers is the main limitations for photocatalytic water-splitting since the photo-excited carriers in such thin layer can quickly recombine. Zhang and coworkers reported that the semiconductors with indirect band gap character can reduce the possibility of recombination of photogenerated electrons and holes.[130]

Aside from monolayer 2D semiconductors, vdWHs

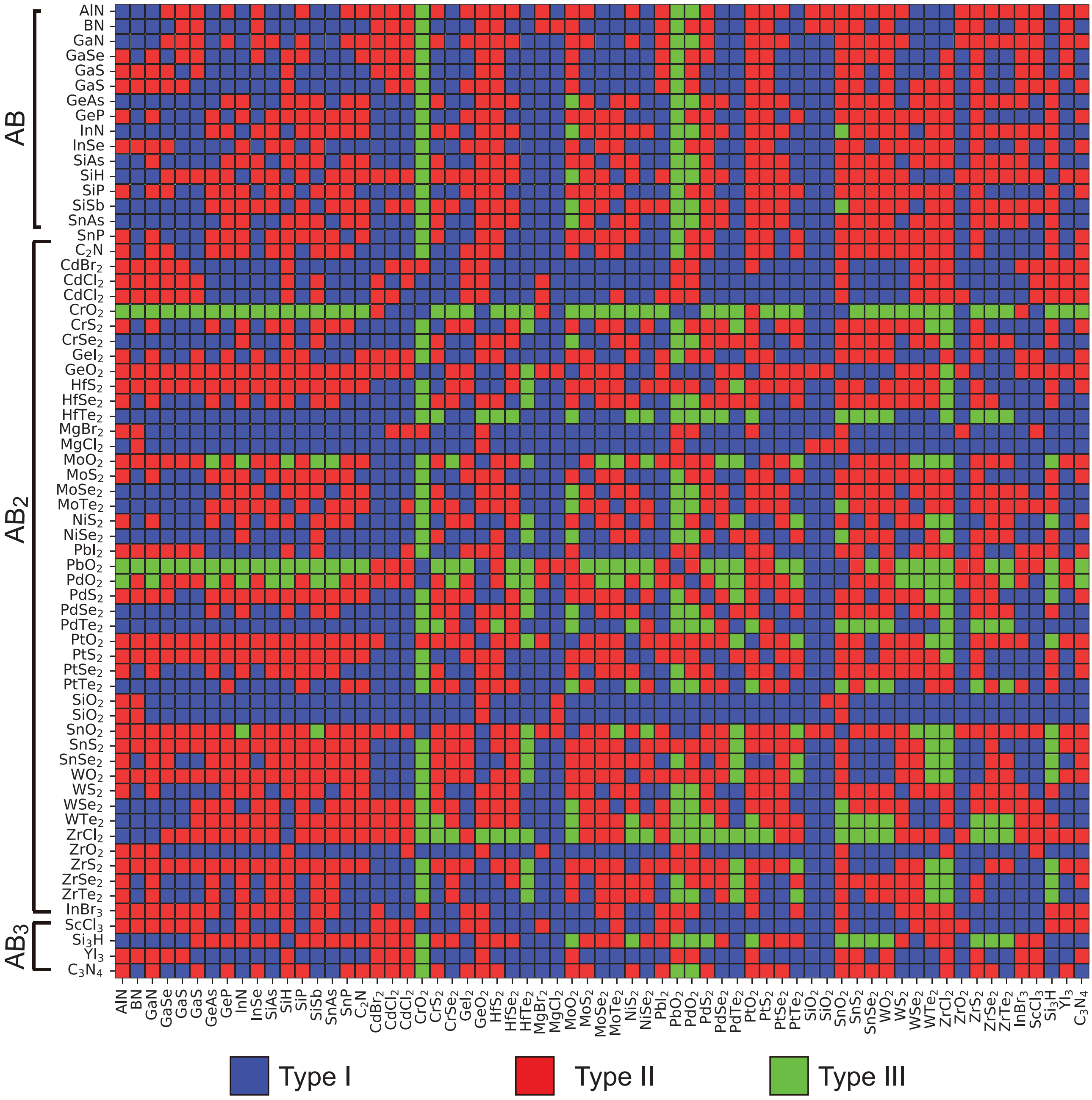

FIG. 18. (Color online) HSE06 calculated periodic table of hexagonal vdWHs. Type I (44.5%), II (44.9%), and III (10.6%) band alignments are represented by blue, red, and green boxes, respectively.

have also been developed as a new avenue to design high-performance photocatalysts for water splitting as discussed in several reviews.[45,46,131–133] Especially, in the type-II heterostructures, the lowest energy states of electrons and holes are on different layers, ensuring efficient separation of photogenerated electrons and holes. This makes them excellent candidates for photocatalysts.[134,135] Zhang *et al.* screened 44 kinds of potential type-II heterojunctions for water splitting under the constraint of suitable band edge positions and similar lattice parameters.[46] Here from more than 20000 possible vdWHs aforementioned, we have screened 927 (pH = 0), 1410 (pH = 7) and 846 (pH = 0∼7) type-II vdWHs which have potential for water splitting photocatalysts. Detailed information are given in the Supplemental Material, respectively. Previous experimental and theoretical studies focus on a limited number of vdWHs, such as C_2N/MoS_2,[136,137] C_2N/WS_2,[137] g-C_3N_4/C_2N,[138]

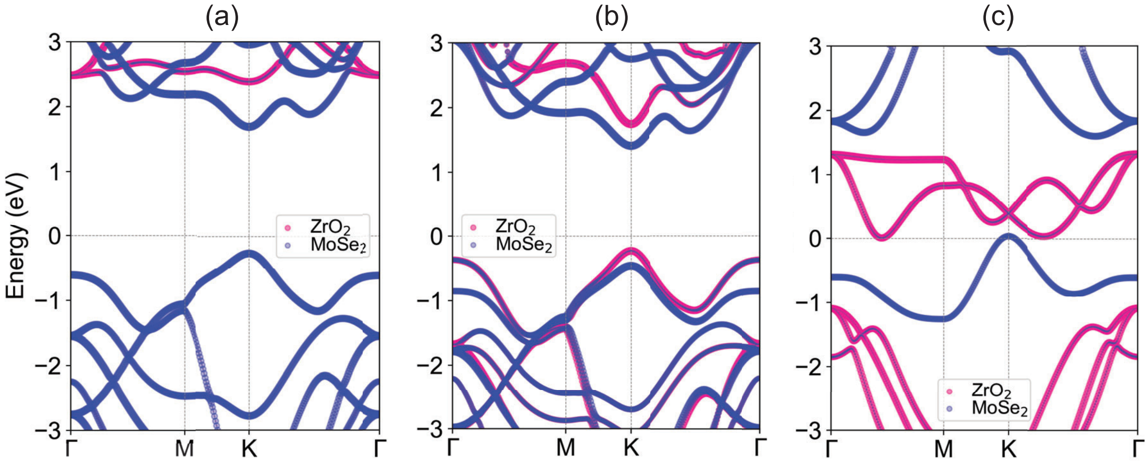

FIG. 19. (Color online) Layer-resolved band structures of (a) $ZrO_2/MoSe_2$ with type I junction, (b) $WSe_2/MoSe_2$ with type II junction and (c) $NiS_2/ZrCl_2$ with type III junction, respectively. The Fermi level is shown with black dashed line.

g-C_3N_4/MoS_2,[139] g-C_3N_4/BP,[140] and InSe/g-C_3N_4.[141] It is expected that out results will serve as a guide to improve the photocatalytic performance of 2D materials.

V. SUMMARY

In conclusion, we have identified 258 2D nonmagnetic semiconductors from near 1000 2D monolayers by performing first-principles high-throughput calculations. The calculated properties include lattice constants, formation energy, Young's modulus, Poisson's ratio, scanning tunnel microscopy, band gap, band structure, anisotropic effective mass, ionization energy and electron affinity. The types of band alignment for more than 20000 van der Waals heterostructures are also provided. Based on the rules of thumb for photocatalytic water splitting, we have screened dozens of monolayer semiconductors and thousands of heterostructures promising for photocatalytic water splitting. We hope that our computational screening database cout stimulate further exploration of 2D semiconductors and heterostructures in photocatalysis, nanoscale devices, and other important applications.

ACKNOWLEDGMENTS

V.W. acknowledges the support of National Natural Science Foundation of China (Grant No. 62174136), Natural Science Basic Research Program of Shaanxi (Program Nos. 2022JQ-063 and 2021JQ-464) and Center for Computational Materials Science, Institute for Materials Research, Tohoku University for the use of MASAMUNE-IMR (Project No.2112SC0503). J.N. were supported by Innovative Science and Technology Initiative for Security Grant Number JPJ004596, ATLA, Japan.

---

[*] wangvei@icloud.com

[†] geng@hainanu.edu.cn

[1] K. S. Novoselov, A. K. Geim, S. V. Morozov, D. Jiang, Y. Zhang, S. V. Dubonos, I. V. Grigorieva, and A. A. Firsov, Science **306**, 666 (2004).

[2] K. Novoselov, A. K. Geim, S. Morozov, D. Jiang, M. Katsnelson, I. Grigorieva, S. Dubonos, and A. Firsov, Nature **438**, 197 (2005).

[3] K. S. Novoselov, D. Jiang, F. Schedin, T. J. Booth, V. V. Khotkevich, S. V. Morozov, and A. K. Geim, PNAS **102**, 10451 (2005).

[4] F. Schwierz, Nature Nanotech. **5**, 487 (2010).

[5] L. Song, Z. Liu, A. L. M. Reddy, N. T. Narayanan, J. Taha-Tijerina, J. Peng, G. Gao, J. Lou, R. Vajtai, and P. M. Ajayan, Adv. Mater. **24**, 4878 (2012).

[6] Q. H. Wang, K. Kalantar-Zadeh, A. Kis, J. N. Coleman, and M. S. Strano, Nat. Nano. **7**, 699 (2012).

[7] Y. Zhang, Y.-W. Tan, H. L. Stormer, and P. Kim, Nature **438**, 201 (2005).

[8] M. Chhowalla, H. S. Shin, G. Eda, L.-J. Li, K. P. Loh, and H. Zhang, Nat. Chem. **5**, 263 (2013).

[9] M. Xu, T. Liang, M. Shi, and H. Chen, Chem. Rev. **113**, 3766 (2013).

[10] S. Z. Butler, S. M. Hollen, L. Cao, Y. Cui, J. A. Gupta, H. R. GutiÃ©rrez, T. F. Heinz, S. S. Hong, J. Huang, A. F. Ismach, E. Johnston-Halperin, M. Kuno, V. V. Plashnitsa, R. D. Robinson, R. S. Ruoff, S. Salahuddin, J. Shan, L. Shi, M. G. Spencer, M. Terrones, W. Windl, and J. E. Goldberger, ACS Nano **7**, 2898 (2013).

[11] Q. Zeng, H. Wang, W. Fu, Y. Gong, W. Zhou, P. M. Ajayan, J. Lou, and Z. Liu, Small **11**, 1868 (2015).

FIG. 20. (Color online) HSE06 calculated band edge positions of 2D candidates relative to the vacuum level for photocatalytic water splitting. The position of the reduction level for H^+ to H_2 and the oxidation potential of H_2 to O_2 are indicated by the dotted and dashed lines, respectively.

[12] S. Balendhran, S. Walia, H. Nili, S. Sriram, and M. Bhaskaran, Small **11**, 640 (2015).

[13] X. Wang, A. M. Jones, K. L. Seyler, V. Tran, Y. Jia, H. Zhao, H. Wang, L. Yang, X. Xu, and F. Xia, Nat. Nano. **10**, 517 (2015).

[14] H. Liu, Y. Du, Y. Deng, and P. D. Ye, Chem. Soc. Rev. **44**, 2732 (2015).

[15] H. Wang, H. Yuan, S. Sae Hong, Y. Li, and Y. Cui, Chem. Soc. Rev. **44**, 2664 (2015).

[16] K. F. Mak, C. Lee, J. Hone, J. Shan, and T. F. Heinz, Phys. Rev. Lett. **105**, 136805 (2010).

[17] B. Radisavljevic, A. Radenovic, J. Brivio, V. Giacometti, and A. Kis, Nat. Nanotechnol. **6**, 147 (2011).

[18] S. Manzeli, D. Ovchinnikov, D. Pasquier, O. V. Yazyev, and A. Kis, Nat. Rev. Mater. **2**, 17033 (2017).

[19] L. Li, Y. Yu, G. J. Ye, Q. Ge, X. Ou, H. Wu, D. Feng, X. H. Chen, and Y. Zhang, Nat. Nanotechnol. **9**, 372 (2014).

[20] H. Liu, A. T. Neal, Z. Zhu, Z. Luo, X. Xu, D. Tománek, and P. D. Ye, ACS Nano **8**, 4033 (2014).

[21] K. Watanabe, T. Taniguchi, and H. Kanda, Nat. Mater. **3**, 404 (2004).

[22] Y. Sugiyama, H. Okamoto, T. Mitsuoka, T. Morikawa, K. Nakanishi, T. Ohta, and H. Nakano, JACS **132**, 5946 (2010).

[23] H. Okamoto, Y. Kumai, Y. Sugiyama, T. Mitsuoka, K. Nakanishi, T. Ohta, H. Nozaki, S. Yamaguchi, S. Shirai, and H. Nakano, JACS **132**, 2710 (2010).

[24] A. O?hare, F. Kusmartsev, and K. Kugel, Nano Lett. **12**, 1045 (2012).

[25] P. Vogt, P. De Padova, C. Quaresima, J. Avila, E. Frantzeskakis, M. C. Asensio, A. Resta, B. Ealet, and G. Le Lay, Phys. Rev. Lett. **108**, 155501 (2012).

[26] E. Bianco, S. Butler, S. Jiang, O. D. Restrepo, W. Windl, and J. E. Goldberger, ACS Nano **7**, 4414 (2013).

[27] L. Li, S.-z. Lu, J. Pan, Z. Qin, Y.-q. Wang, Y. Wang, G.-y. Cao, S. Du, and H.-J. Gao, Adv. Mater. **26**, 4820 (2014).

[28] F.-f. Zhu, W.-j. Chen, Y. Xu, C.-l. Gao, D.-d. Guan, C.-h. Liu, D. Qian, S.-C. Zhang, and J.-f. Jia, Nat. Mater. **14**, 1020 (2015).

[29] T. Inoshita, S. Jeong, N. Hamada, and H. Hosono, Phys. Rev. X **4**, 031023 (2014).

[30] M. Ashton, J. Paul, S. B. Sinnott, and R. G. Hennig, Phys. Rev. Lett. **118**, 106101 (2017).

[31] A. Jain, S. P. Ong, G. Hautier, W. Chen, W. D. Richards, S. Dacek, S. Cholia, D. Gunter, D. Skinner, G. Ceder, and K. A. Persson, APL Mater. **1**, 011002 (2013).

[32] K. Choudhary, I. Kalish, R. Beams, and F. Tavazza, Sci. Rep. **7**, 5179 (2017).

[33] G. Cheon, K.-A. N. Duerloo, A. D. Sendek, C. Porter, Y. Chen, and E. J. Reed, Nano Lett. **17**, 1915 (2017).

[34] N. Mounet, M. Gibertini, P. Schwaller, D. Campi, A. Merkys, A. Marrazzo, T. Sohier, I. E. Castelli, A. Cepellotti, G. Pizzi, and N. Marzari, Nat. Nanotechnol. **13**, 246 (2018).

[35] S. Haastrup, M. Strange, M. Pandey, T. Deilmann, P. S. Schmidt, N. F. Hinsche, M. N. Gjerding, D. Torelli, P. M. Larsen, A. C. Riis-Jensen, J. Gath, K. W. Jacobsen, J. JÃžrgen Mortensen, T. Olsen, and K. S. Thygesen, 2D Mater. **5**, 042002 (2018).

[36] J. Zhou, L. Shen, M. D. Costa, K. A. Persson, S. P. Ong, P. Huck, Y. Lu, X. Ma, Y. Chen, H. Tang, and Y. P. Feng, Scientific Data **6**, 86 (2019).

[37] A. K. Geim and I. V. Grigorieva, Nature **499**, 419 (2013).

[38] K. S. Novoselov, A. Mishchenko, A. Carvalho, and A. H. C. Neto, Science **353**, aac9439 (2016).

[39] Y. Liu, N. O. Weiss, X. Duan, H.-C. Cheng, Y. Huang, and X. Duan, Nat. Rev. Mater. **1**, 16042 (2016).

[40] F. Xia, H. Wang, D. Xiao, M. Dubey, and A. Ramasubramaniam, Nat. Photonics **8**, 899 (2014).

[41] J. F. Sierra, J. Fabian, R. K. Kawakami, S. Roche, and S. O. Valenzuela, Nat. Nanotechnol. **16**, 856 (2021).

[42] Y. Cao, V. Fatemi, S. Fang, K. Watanabe, T. Taniguchi, E. Kaxiras, and P. Jarillo-Herrero, Nature **556**, 43 (2018).

[43] E. Pomerantseva and Y. Gogotsi, Nat. Energy **2**, 17089 (2017).

[44] D. Deng, K. S. Novoselov, Q. Fu, N. Zheng, Z. Tian, and X. Bao, Nat. Nanotechnol. **11**, 218 (2016).

[45] A. K. Singh, K. Mathew, H. L. Zhuang, and R. G. Hennig, J. Phys. Chem. Lett. **6**, 1087 (2015).

[46] X. Zhang, Z. Zhang, D. Wu, X. Zhang, X. Zhao, and Z. Zhou, Small Methods **2**, 1700359 (2018).

[47] P. Ganguly, M. Harb, Z. Cao, L. Cavallo, A. Breen, S. Dervin, D. D. Dionysiou, and S. C. Pillai, ACS Energy Letters **4**, 1687 (2019).

[48] G. Kresse and J. Furthmüller, Phys. Rev. B **54**, 11169 (1996).

[49] G. Kresse and J. Furthmüller, Comput. Phys. Sci. **6**, 15 (1996).

[50] P. E. Blöchl, Phys. Rev. B **50**, 17953 (1994).

[51] G. Kresse and D. Joubert, Phys. Rev. B **59**, 1758 (1999).

[52] J. P. Perdew, K. Burke, and M. Ernzerhof, Phys. Rev. Lett. **77**, 3865 (1996).

[53] A. D. Becke, J. Chem. Phys. **98**, 1372 (1993).

[54] J. Heyd, G. E. Scuseria, and M. Ernzerhof, J. Chem. Phys. **118**, 8207 (2003).

[55] J. P. Perdew, M. Ernzerhof, and K. Burke, J. Chem. Phys. **105**, 9982 (1996).

[56] J. Paier, M. Marsman, K. Hummer, G. Kresse, I. C. Gerber, and J. G. Angyan, J. Chem. Phys. **124**, 154709 (2006).

[57] A. V. Krukau, O. A. Vydrov, A. F. Izmaylov, and G. E. Scuseria, J. Chem. Phys. **125**, 224106 (2006).

[58] M. Marsman, J. Paier, A. Stroppa, and G. Kresse, J. Phys.: Condens. Matter **20**, 064201 (2008).

[59] S. Grimme, J. Comput. Chem. **27**, 1787 (2006).

[60] T. Bučko, J. Hafner, S. Lebègue, and J. Ángyán, J. Phys. Chem. A **114**, 11814 (2010).

[61] H. J. Monkhorst and J. D. Pack, Phys. Rev. B **13**, 5188 (1976).

[62] V. Wang, N. Xu, J.-C. Liu, G. Tang, and W.-T. Geng, Comput. Phys. Commun. **267**, 108033 (2021).

[63] J. Heyd, J. E. Peralta, G. E. Scuseria, and R. L. Martin, J. Chem. Phys. **123**, 174101 (2005).

[64] A. J. Mannix, X.-F. Zhou, B. Kiraly, J. D. Wood, D. Alducin, B. D. Myers, X. Liu, B. L. Fisher, U. Santiago, J. R. Guest, M. J. Yacaman, A. Ponce, A. R. Oganov, M. C. Hersam, and N. P. Guisinger, Science **350**, 1513 (2015).

[65] J. T. Paul, A. K. Singh, Z. Dong, H. Zhuang, B. C. Revard, B. Rijal, M. Ashton, A. Linscheid, M. Blonsky, D. Gluhovic, J. Guo, and R. G. Hennig, J. Phys.: Condens. Matter **29**, 473001 (2017).

[66] O. I. Malyi, K. V. Sopiha, and C. Persson, ACS Appl. Mater. Interfaces **11**, 24876 (2019).

[67] M. Pandey and K. W. Jacobsen, Phys. Rev. B **91**, 235201 (2015).

[68] W. Voigt *et al.*, *Lehrbuch der kristallphysik*, Vol. 962 (Teubner Leipzig, 1928).

[69] M. Maździarz, 2D Mater. **6**, 048001 (2019).

[70] M. Born and K. Huang, "Dynamic theory of crystal lattice, clarendon," (1954).

[71] K. Parlinski, Z. Q. Li, and Y. Kawazoe, Phys. Rev. Lett. **78**, 4063 (1997).

[72] S. Baroni, S. de Gironcoli, A. Dal Corso, and P. Giannozzi, Rev. Mod. Phys. **73**, 515 (2001).

[73] A. Togo and I. Tanaka, Scr. Mater. **108**, 1 (2015).

[74] E. S. Penev, A. Kutana, and B. I. Yakobson, Nano Lett. **16**, 2522 (2016).

[75] G. J. Martyna, M. L. Klein, and M. Tuckerman, J. Chem. Phys. **97**, 2635 (1992).

[76] C. Ataca, H. ?ahin, and S. Ciraci, J. Phys. Chem. C **116**, 8983 (2012).

[77] F. A. Rasmussen and K. S. Thygesen, J. Phys. Chem. C **119**, 13169 (2015).

[78] R. Li, Q. Shao, E. Gao, and Z. Liu, Extreme Mech. Lett. **34**, 100615 (2020).

[79] R. Hill, Proceedings of the Physical Society. Section A **65**, 349 (1952).

[80] D. PacilÃ©, J. C. Meyer, Ã. Ã. Girit, and A. Zettl, Appl. Phys. Lett. **92**, 133107 (2008).

[81] J. O. Island, M. Barawi, R. Biele, A. AlmazÃ¡n, J. M. Clamagirand, J. R. Ares, C. SÃ¡nchez, H. S. J. van der Zant, J. V. Ãlvarez, R. D'Agosta, I. J. Ferrer, and A. Castellanos?Gomez, Adv. Mater. **27**, 2595 (2015).

[82] C. Lee, X. Wei, J. W. Kysar, and J. Hone, Science **321**, 385 (2008).

[83] F. Liu, P. Ming, and J. Li, Phys. Rev. B **76**, 064120 (2007).

[84] C. Jasiukiewicz, T. Paszkiewicz, and S. Wolski, physica status solidi (b) **245**, 562 (2008).

[85] C. Jasiukiewicz, T. Paszkiewicz, and S. Wolski, physica status solidi (b) **247**, 1247 (2010).

[86] A. Falin, Q. Cai, E. J. G. Santos, D. Scullion, D. Qian, R. Zhang, Z. Yang, S. Huang, K. Watanabe, T. Taniguchi, M. R. Barnett, Y. Chen, R. S. Ruoff, and L. H. Li, Nat. Commun. **8**, 15815 (2017).

[87] L. Wang, A. Kutana, X. Zou, and B. I. Yakobson, Nanoscale **7**, 9746 (2015).

[88] J. Kang, H. Sahin, and F. M. Peeters, Phys. Chem. Chem. Phys. **17**, 27742 (2015).

[89] W. Yang, Z.-M. Li, W. Shi, B.-H. Xie, and M.-B. Yang, J. Mater. Sci. **39**, 3269 (2004).

[90] G. N. Greaves, A. L. Greer, R. S. Lakes, and T. Rouxel, Nature Materials **10**, 823 (2011).

[91] C. Huang and L. Chen, Adv. Mater. **28**, 8079 (2016).

[92] J.-W. Jiang and H. S. Park, Nat. Commun. **5**, 4727 (2014).

[93] Y. Du, J. Maassen, W. Wu, Z. Luo, X. Xu, and P. D. Ye, Nano Lett. **16**, 6701 (2016).

[94] J. Han, J. Xie, Z. Zhang, D. Yang, M. Si, and D. Xue, Appl. Phys. Express **8**, 041801 (2015).

[95] Y. Jin, X. Li, and J. Yang, Phys. Chem. Chem. Phys. **17**, 18665 (2015).

[96] V. Wang, Y. Kawazoe, and W. T. Geng, Phys. Rev. B **91**, 045433 (2015).

[97] D. Jun, L. Ming, and Z. X. Cheng, WIREs Comput. Mol. Sci. **6**, 211 (2016).

[98] Y. Cai, G. Zhang, and Y.-W. Zhang, Scientific Reports **4**, 6677 (2014).

[99] V. O. Özçelik, J. G. Azadani, C. Yang, S. J. Koester, and T. Low, Phys. Rev. B **94**, 035125 (2016).

[100] J. Kang, S. Tongay, J. Zhou, J. Li, and J. Wu, Appl. Phys. Lett. **102**, 012111 (2013).

[101] J. Dai and X. C. Zeng, Angew. Chem. Int. Ed. **54**, 7572 (2015).

[102] L. Matthes, O. Pulci, and F. Bechstedt, New J. Phys. **16**, 105007 (2014).

[103] L. Matthes, O. Pulci, and F. Bechstedt, Phys. Rev. B **94**, 205408 (2016).

[104] B. Adolph, V. I. Gavrilenko, K. Tenelsen, F. Bechstedt, and R. Del Sole, Phys. Rev. B **53**, 9797 (1996).

[105] G. Binnig, H. Rohrer, C. Gerber, and E. Weibel, Phys. Rev. Lett. **49**, 57 (1982).

[106] J. Tersoff and D. R. Hamann, Phys. Rev. B **31**, 805 (1985).

[107] Q. Yu, L. A. Jauregui, W. Wu, R. Colby, J. Tian, Z. Su, H. Cao, Z. Liu, D. Pandey, D. Wei, T. F. Chung, P. Peng, N. P. Guisinger, E. A. Stach, J. Bao, S.-S. Pei, and Y. P. Chen, Nat. Mater. **10**, 443 (2011).

[108] B. Kiraly, N. Hauptmann, A. N. Rudenko, M. I. Katsnelson, and A. A. Khajetoorians, Nano Lett. **17**, 3607 (2017).

[109] T.-A. Chen, C.-P. Chuu, C.-C. Tseng, C.-K. Wen, H.-S. P. Wong, S. Pan, R. Li, T.-A. Chao, W.-C. Chueh, Y. Zhang, Q. Fu, B. I. Yakobson, W.-H. Chang, and L.-J. Li, Nature **579**, 219 (2020).

[110] F. Withers, O. Del Pozo-Zamudio, A. Mishchenko, A. P. Rooney, A. Gholinia, K. Watanabe, T. Taniguchi, S. J. Haigh, A. K. Geim, A. I. Tartakovskii, and K. S. Novoselov, Nat. Mater. **14**, 301 (2015).

[111] X. Hong, J. Kim, S.-F. Shi, Y. Zhang, C. Jin, Y. Sun, S. Tongay, J. Wu, Y. Zhang, and F. Wang, Nat. Nanotechnol. **9**, 682 (2014).

[112] M. M. Furchi, A. Pospischil, F. Libisch, J. BurgdÃ¶rfer, and T. Mueller, Nano Lett. **14**, 4785 (2014).

[113] Y.-C. Lin, R. K. Ghosh, R. Addou, N. Lu, S. M. Eichfeld, H. Zhu, M.-Y. Li, X. Peng, M. J. Kim, L.-J. Li, R. M. Wallace, S. Datta, and J. A. Robinson, Nat. Commun. **6**, 7311 (2015).

[114] M. Massicotte, P. Schmidt, F. Vialla, K. G. SchÃ€dler, A. Reserbat-Plantey, K. Watanabe, T. Taniguchi, K. J. Tielrooij, and F. H. L. Koppens, Nat. Nanotechnol **11**, 42 (2016).

[115] R. Yan, S. Fathipour, Y. Han, B. Song, S. Xiao, M. Li, N. Ma, V. Protasenko, D. A. Muller, D. Jena, and H. G. Xing, Nano Lett. **15**, 5791 (2015).

[116] J. Shim, S. Oh, D.-H. Kang, S.-H. Jo, M. H. Ali, W.-Y. Choi, K. Heo, J. Jeon, S. Lee, M. Kim, Y. J. Song, and J.-H. Park, Nat .Commun. **7**, 13413 (2016).

[117] R. Anderson, IBM J. Res. Dev. **4**, 283 (1960).

[118] K. L. Seyler, P. Rivera, H. Yu, N. P. Wilson, E. L. Ray, D. G. Mandrus, J. Yan, W. Yao, and X. Xu, Nature **567**, 66 (2019).

[119] Z. Shi, X. Wang, Y. Sun, Y. Li, and L. Zhang, Semiconductor Science and Technology **33**, 093001 (2018).

[120] X. Wu, X. Chen, R. Yang, J. Zhan, Y. Ren, and K. Li, Small **18**, 2105877 (2022).

[121] V. Chakrapani, J. C. Angus, A. B. Anderson, S. D. Wolter, B. R. Stoner, and G. U. Sumanasekera, Science **318**, 1424 (2007).

[122] M. G. Walter, E. L. Warren, J. R. McKone, S. W. Boettcher, Q. Mi, E. A. Santori, and N. S. Lewis, Chem. Rev. **110**, 6446 (2010).

[123] X. Wang, K. Maeda, A. Thomas, K. Takanabe, G. Xin, J. M. Carlsson, K. Domen, and M. Antonietti, Nature Materials **8**, 76 (2009).

[124] J. Mahmood, E. K. Lee, M. Jung, D. Shin, I.-Y. Jeon, S.-M. Jung, H.-J. Choi, J.-M. Seo, S.-Y. Bae, S.-D. Sohn, N. Park, J. H. Oh, H.-J. Shin, and J.-B. Baek, Nat. Commun. **6**, 6486 (2015).

[125] F. Jaramillo Thomas, P. JÃžrgensen Kristina, B. Jacob, H. Nielsen Jane, H. Sebastian, and C. Ib, Science **317**, 100 (2007).

[126] W. Hu, L. Lin, R. Zhang, C. Yang, and J. Yang, J. Am. Chem. Soc. **139**, 15429 (2017).

[127] M. Qiao, J. Liu, Y. Wang, Y. Li, and Z. Chen, J. Am. Chem. Soc. **140**, 12256 (2018).

[128] T. Yu, C. Wang, X. Yan, G. Yang, and U. Schwingenschlögl, J. Phys. Chem. Lett. **12**, 2464 (2021).

[129] B. Wang, X. Niu, Y. Ouyang, Q. Zhou, and J. Wang, J. Phys. Chem. Lett. **9**, 487 (2018).

[130] P. Zhang, J. Zhang, and J. Gong, Chem. Soc. Rev. **43**, 4395 (2014).

[131] T. A. Shifa, F. Wang, Y. Liu, and J. He, Adv. Mater. **31**, 1804828 (2019).

[132] G. Wang, J. Chang, W. Tang, W. Xie, and Y. S. Ang, J. Phys. D: Appl. Phys. **55**, 293002 (2022).

[133] M. Jakhar, A. Kumar, P. K. Ahluwalia, K. Tankeshwar, and R. Pandey, "Engineering 2d materials for photocatalytic water-splitting from a theoretical perspective," (2022).

[134] Y. Wang, Q. Wang, X. Zhan, F. Wang, M. Safdar, and J. He, Nanoscale **5**, 8326 (2013).

[135] J. Low, J. Yu, M. Jaroniec, S. Wageh, and A. A. Al-Ghamdi, Adv. Mater. **29**, 1601694 (2017).

[136] Z. Guan, C.-S. Lian, S. Hu, S. Ni, J. Li, and W. Duan, J. Phys. Chem. C **121**, 3654 (2017).

[137] R. Kumar, D. Das, and A. K. Singh, J. Catal. **359**, 143 (2018).

[138] H. Wang, X. Li, and J. Yang, ChemPhysChem **17**, 2100 (2016).

[139] J. Wang, Z. Guan, J. Huang, Q. Li, and J. Yang, J. Mater. Chem. A **2**, 7960 (2014).

[140] J. Ran, W. Guo, H. Wang, B. Zhu, J. Yu, and S.-Z. Qiao, Adv. Mater. **30**, 1800128 (2018).

[141] C. He, J. H. Zhang, W. X. Zhang, and T. T. Li, J. Phys. Chem. Lett. **10**, 3122 (2019).